

Unified bulk mobility model for low- and high-field transport in silicon

Andreas Schenk^{a)}

Swiss Federal Institute of Technology, Integrated Systems Laboratory, Gloriastrasse 35, CH-8092 Zürich, Switzerland

(Received 3 April 1995; accepted for publication 26 September 1995)

An analytical bulk mobility model for hydrodynamic transport equations is developed from a microscopic level and designed for silicon device simulation. Applying Kohler's variational method extended to the regime of nonlinear transport yields the general expression for the mobility as function of carrier temperature, lattice temperature, and doping. Assuming a nonparabolic, isotropic band model and a heated Maxwellian allows for the analytical calculation of the collision integrals. A nonelastic approximation for intravalley acoustic-phonon scattering is proposed, which improves the model in the low-temperature range. Intervalley scattering is treated in a one-mode, equipartition approximation. Here, an accurate analytical approach for all carrier temperatures is derived. For impurity scattering the Brooks-Herring theory is used including Fermi statistics and the effect of dispersive screening. The influence of other effects like anisotropic valleys and perturbation of the density of states by heavy doping are discussed quantitatively. Despite the oversimplified band structure, all essential features of the measured mobility in silicon can be reproduced except in the heavy doping range. The adjusted deformation potentials coincide with estimated sums of the corresponding sets used in full-band Monte Carlo simulation. The method has the potential of an extension to the Si-SiO₂ system. © 1996 American Institute of Physics. [S0021-8979(96)09701-5]

I. INTRODUCTION

The hydrodynamic (HD) transport scheme^{1,2} has become a standard device simulation tool with the capability for describing nonlocal and nonstationary phenomena. Computation times compare favorably with those of Monte Carlo (MC) simulations³ and methods based on a spherical-harmonics (SH) expansion of the Boltzmann transport equation (BTE).⁴ Thus, it is suitable also for more sophisticated applications like power-device, multi-device or 3D-device simulations. Using HD results as initial solution for the SH and MC methods is a forthcoming issue.

The HD transport equations contain momentum relaxation times (RTs) as function of carrier temperature (or carrier energy), depending on the particular method of moments. Usually, these quantities are obtained from bulk homogeneous MC simulations. The lack of this procedure is obvious: it is hardly possible to find complete tables or fit functions for the mobility depending on average carrier temperature, lattice temperature and doping. But even then, there remains the problem of the mutual influence caused by lattice temperature profiles (hot spots), impurity density profiles and field peaks met in modern devices. Furthermore, the limitations of present-day MC programs which are calibrated to pure and homogeneous silicon, do not allow to yield reliable mobilities near interfaces and in heavily doped regions, whereas in the HD scheme heuristic models can be used.

An alternative way is to calculate the mobility as a function of carrier temperature T_c , lattice temperature T_L , and impurity density N_{imp} *analytically* from a microscopic level. If the calibration of parameters using experimental and MC data is done on the same microscopic level (deformation po-

tentials, phonon energies), one can hope that a broad range of conditions can be covered by such a model. It is the particular difficulty in this project to describe the mobility in both high-field regions and heavily doped regions within one model, which is however necessary for the purpose of device simulation. This difficulty arises from the inability to use a realistic band structure model for high energies and a realistic density of states (DOS) for heavily doped silicon. In order to achieve an analytical result, we will restrict ourselves to an isotropic, nonparabolic one-band model. Despite its simplicity, high-field effects like drift-velocity saturation can be obtained correctly adjusting the nonparabolicity parameter. The most demanding problem is to fit the impurity scattering in heavily doped regions: as will be shown, for $N_{imp} > 10^{19}$ cm⁻³, the measured mobility can be reproduced only phenomenologically.

The paper is organized as follows: in Section II the analytical model of the electron mobility is derived using Kohler's variational method for the BTE and assuming a heated Maxwellian for the even part of the distribution function. The scattering mechanisms are listed and the analytical integrations to obtain the partial mobilities are briefly outlined. Intravalley acoustic phonon scattering is treated in a non-elastic approach. Various levels of complexity in describing impurity scattering are discussed. Section III compares the model with experimental data and MC results, and describes the parameter fitting. The essential features of the model, i.e. the dependencies on ambient temperature, carrier temperature and doping are demonstrated. The hole mobility model is derived in Section IV. In Section V we present some simulation results obtained with the new model, and conclusions are given in Section VI.

^{a)}Electronic mail: schenk@iis.ee.ethz.ch

II. ANALYTICAL MODEL OF THE ELECTRON MOBILITY

A. Variational method with a heated Maxwellian

The subject of this paper is a bulk mobility model for HD transport equations as they are used for the numerical simulation of silicon devices. No spatial inhomogeneities, as for the channel mobility in MOSFETs, will be considered here. The derivation will be based on a variational method (Kohler's method^{5,6}) to solve the BTE. In principle, this method allows to treat all scattering mechanisms without the assumptions which are necessary for the application of the relaxation time approximation (RTA). For the bulk case and transients much slower than the inverse total scattering rate we can restrict ourselves to the time- and space-independent BTE

$$\frac{\mathbf{F}}{\hbar} \cdot \nabla_{\mathbf{k}} f(\mathbf{k}) = \sum_{\mathbf{k}'} \{ [1 - f(\mathbf{k})] W_{\mathbf{k}\mathbf{k}'} f(\mathbf{k}') - [1 - f(\mathbf{k}')] W_{\mathbf{k}'\mathbf{k}} f(\mathbf{k}) \}. \quad (1)$$

Here \mathbf{F} denotes the electric force and $W_{\mathbf{k}\mathbf{k}'}$ the total first-order transition probability from a state with momentum \mathbf{k}' into a state with momentum \mathbf{k} . For the distribution function $f(\mathbf{k})$ the so-called ‘‘diffusion approximation’’⁷ is modified in the following way:⁸ $f(\mathbf{k})$ is split into an even part $f^{(0)}(\mathbf{k})$ and an odd part $f^{(1)}(\mathbf{k})$, where in contrast to the regime of Ohm's law $f^{(0)}(\mathbf{k})$ is a zeroth order approximation for the *non-equilibrium* distribution function. We assume that the heated, non-displaced Maxwellian

$$f^{(0)}(\mathbf{k}) = \frac{n}{N_c} \exp\left(-\frac{E_{\mathbf{k}}(\alpha E_{\mathbf{k}} + 1)}{k_B T_n}\right) \quad (2)$$

can represent such an approximation even at high electric fields. In Eq. (2) n denotes the electron density, N_c the total effective density of band states, T_n the electron temperature, α the nonparabolicity parameter, and $E_{\mathbf{k}}$ the band dispersion. $f^{(0)}(\mathbf{k})$ is even, since $E_{\mathbf{k}} = E_{-\mathbf{k}}$. We note that $f^{(0)}(\mathbf{k})$ represents the distribution in one valley; the zero- and second-order moments yield

$$\frac{1}{(2\pi)^3} \int d^3\mathbf{k} f^{(0)}(\mathbf{k}) = \frac{n}{6}, \quad (3)$$

$$\frac{1}{(2\pi)^3} \int d^3\mathbf{k} \frac{\hbar^2 \mathbf{k}^2}{2m_{dn}} f^{(0)}(\mathbf{k}) = \frac{n}{6} \times \frac{3}{2} k_B T_n \quad (4)$$

for the isotropic band structure model which will be introduced below. If the motion of the particles retains its random character also at high T_n , the distribution function remains weakly anisotropic in \mathbf{k} -space, and the odd part $f^{(1)}(\mathbf{k})$ can be regarded as a ‘‘small correction.’’ This concept seems to be adequate for the various kinds of HD and thermodynamic (TD) transport models, but must be expected to fail in situations where the electron motion becomes streaming. The latter happens, e.g., in deep sub-micron MOSFETs near the drain junction, where the ratio of drift to root-mean square velocity reaches high values. Fig. 1 shows that Eq. (2) approximates well the distribution function from a full-band MC simulation⁹ up to electron temperatures of about 1500 K.

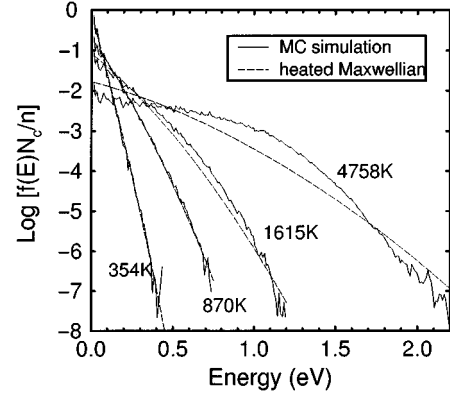


FIG. 1. Normalized distribution function $f(E)N_c/n$ of electrons in silicon. The solid lines are results of a full-band MC simulation (see Ref. 9), the dashed lines represent the heated Maxwellian Eq. (2) with average carrier temperatures from the MC simulation and $\alpha = 0.5/\text{eV}$.

For higher T_n a strong redistribution occurs from low to high carrier energies, which cannot be reflected by the heated Maxwellian. At room temperature, carrier densities larger than 10^{19}cm^{-3} require to use degenerate statistics. In the case of a degenerate electron gas the heated Maxwellian has to be replaced by a ‘‘heated Fermi distribution’’

$$f^{(0)}(\mathbf{k}) = \left[\exp\left(\frac{E_{\mathbf{k}}(\alpha E_{\mathbf{k}} + 1)}{k_B T_n} - \eta_n\right) + 1 \right]^{-1} \quad (5)$$

with $\eta_n = (E_{F,n} - E_c)/k_B T_n$ ($E_{F,n}$ —quasi Fermi energy, E_c —band edge). In this case, the bulk mobility is fully determined by impurity scattering, hence we will consider the case of degeneracy only there.

The assumption $f^{(1)}(\mathbf{k}) \ll f^{(0)}(\mathbf{k})$ allows for a linearization of the BTE in $f^{(1)}$

$$\begin{aligned} \frac{\mathbf{F}}{\hbar} \cdot \nabla_{\mathbf{k}} f^{(0)}(\mathbf{k}) &= \sum_{\mathbf{k}'} (P_{\mathbf{k}\mathbf{k}'} - P_{\mathbf{k}'\mathbf{k}}) \\ &+ \sum_{\mathbf{k}'} \left(\frac{P_{\mathbf{k}\mathbf{k}'}}{f^{(0)}(\mathbf{k}')} + \frac{P_{\mathbf{k}'\mathbf{k}}}{1 - f^{(0)}(\mathbf{k}')} \right) f^{(1)}(\mathbf{k}') \\ &- f^{(1)}(\mathbf{k}) \sum_{\mathbf{k}'} \left(\frac{P_{\mathbf{k}'\mathbf{k}}}{f^{(0)}(\mathbf{k})} + \frac{P_{\mathbf{k}\mathbf{k}'}}{1 - f^{(0)}(\mathbf{k})} \right), \quad (6) \end{aligned}$$

where we have introduced the collision operator

$$P_{\mathbf{k}\mathbf{k}'} = [1 - f^{(0)}(\mathbf{k})] f^{(0)}(\mathbf{k}') W_{\mathbf{k}\mathbf{k}'}. \quad (7)$$

In thermodynamic equilibrium ($T_n = T_L$, T_L —lattice temperature), due to the principle of detailed balance $P_{\mathbf{k}\mathbf{k}'} = P_{\mathbf{k}'\mathbf{k}}$ holds. Here, $P_{\mathbf{k}\mathbf{k}'}$ is no longer symmetrical, since $f^{(0)}(\mathbf{k})$ represents a state far from equilibrium. However, the symmetry of the collision operator in the BTE is a precondition for the variational method. To obtain a symmetrical collision operator we write as usual

$$\begin{aligned} f^{(1)}(\mathbf{k}) &= -\Phi(\mathbf{k}) \frac{\partial f^{(0)}}{\partial E_{\mathbf{k}}} \\ &= \frac{1}{k_B T_n} \tilde{\Phi}(\mathbf{k}) [1 - f^{(0)}(\mathbf{k})] f^{(0)}(\mathbf{k}), \quad (8) \end{aligned}$$

with $\tilde{\Phi}(\mathbf{k}) = \Phi(\mathbf{k})(1 + 2\alpha E_{\mathbf{k}})$ and rewrite the BTE by intro-

ducing symmetrical and antisymmetrical operators $\Pi_{kk'}^s$ and $\Pi_{kk'}^a$, respectively

$$\begin{aligned} \mathbf{F} \cdot \mathbf{v}_g(\mathbf{k}) \frac{\partial f^{(0)}}{\partial E_{\mathbf{k}}} - \sum_{k'} (P_{kk'} - P_{k'k}) \\ = \frac{1}{2k_B T_n} \sum_{k'} \{ \Pi_{kk'}^s [\Phi(\mathbf{k}') - \Phi(\mathbf{k})] \\ + \Pi_{kk'}^a [\Phi(\mathbf{k}') + \Phi(\mathbf{k})] \}, \end{aligned} \quad (9)$$

where $\mathbf{v}_g(\mathbf{k})$ denotes the group velocity and

$$\Pi_{kk'}^s = (\tilde{P}_{kk'} \pm \tilde{P}_{k'k}) - (P_{kk'} - P_{k'k}) [\tilde{f}^{(0)}(\mathbf{k}') \mp \tilde{f}^{(0)}(\mathbf{k})]. \quad (10)$$

In (10) $\tilde{f}^{(0)}(\mathbf{k}) = f^{(0)}(\mathbf{k})(1 + 2\alpha E_{\mathbf{k}})$ and $\tilde{P}_{kk'} = P_{kk'}(1 + 2\alpha E_{\mathbf{k}'})$. It is obvious from Eq. (8) that the assumption $f^{(1)}(\mathbf{k}) \ll f^{(0)}(\mathbf{k})$ is equivalent to $\Phi(\mathbf{k}) \ll k_B T_n$. Therefore, we can neglect both $\Pi_{kk'}^a$ and the second term of $\Pi_{kk'}^s$, which is negligible in the case of Boltzmann statistics anyway. All these terms are proportional to $\Phi(\mathbf{k})/(2k_B T_n)$ and, therefore, can be neglected as compared to $(P_{kk'} - P_{k'k})$ on the left-hand side of Eq. (9). The BTE now can be written as operator equation

$$\varphi_1 + \varphi_2 = \Pi^s \Phi \quad (11)$$

with

$$\varphi_1 = \mathbf{F} \cdot \mathbf{v}_g(\mathbf{k}) \frac{\partial f^{(0)}}{\partial E_{\mathbf{k}}}, \quad (12)$$

$$\varphi_2 = \sum_{k'} (P_{kk'} - P_{k'k}), \quad (13)$$

$$\Pi^s \Phi = \frac{1}{2k_B T_n} \sum_{k'} (\tilde{P}_{kk'} + \tilde{P}_{k'k}) [\Phi(\mathbf{k}') - \Phi(\mathbf{k})]. \quad (14)$$

With the symmetrical collision operator in (11) the variational method is straightforward. Applying the electric field in z-direction and taking into account only the first-order term in the linear combination of $\Phi(\mathbf{k})$ with trial functions k_z^n : $\Phi(\mathbf{k}) = a_0 k_z$, the BTE is transformed into the algebraic equation

$$b_0 = d_{00} a_0 \quad (15)$$

with

$$b_0 = (\varphi_1 + \varphi_2, k_z), \quad d_{00} = (k_z, \Pi^s k_z), \quad (16)$$

where (φ, ξ) denotes the inner product $1/\Omega \sum_{\mathbf{k}} \varphi(\mathbf{k}) \xi(\mathbf{k})$ (Ω —crystal volume). On the other hand, the electron conductivity is defined by

$$\begin{aligned} \sigma_n = \frac{e j_z}{F_z} &= \frac{2e^2}{\Omega F_z} \sum_{\mathbf{k}} f^{(1)}(\mathbf{k}) v_{g,z}(\mathbf{k}) \\ &= -\frac{2e^2}{\Omega F_z} \sum_{\mathbf{k}} \Phi(\mathbf{k}) \frac{\partial f^{(0)}}{\partial E_{\mathbf{k}}} v_{g,z}(\mathbf{k}) \\ &= -\frac{2e^2}{F_z^2} (\Phi, \varphi_1). \end{aligned} \quad (17)$$

Inserting $\Phi(\mathbf{k}) = a_0 k_z$ and using (15)–(16) we obtain

$$\sigma_n = -\frac{2e^2}{F_z^2 d_{00}} [(\varphi_1, k_z)^2 + (\varphi_1, k_z)(\varphi_2, k_z)]. \quad (18)$$

It is easily proven that

$$(\varphi_1, k_z) = -\frac{F_z}{2\hbar} n \quad (19)$$

without any assumptions on the band structure. The second term in Eq. (18) contains the inner product

$$\begin{aligned} (\varphi_2, k_z) &= -\frac{1}{\Omega} \sum_{kk'} (P_{kk'} - P_{k'k}) k_z \\ &= -\frac{1}{\Omega} \sum_{kk'} P_{kk'} (k_z - k'_z). \end{aligned} \quad (20)$$

All scattering mechanisms discussed in the following section have transition probabilities with the property $P_{kk'} = P_{-k-k'}$. Therefore, (φ_2, k_z) vanishes.

According to (18) and (19) the mobility is determined by the quantity d_{00} which contains the whole microscopic information. With (14) and (16) it takes the form

$$\begin{aligned} d_{00} &= -\frac{1}{4\Omega k_B T_n} \sum_{kk'} (\tilde{P}_{kk'} + \tilde{P}_{k'k}) (k'_z - k_z)^2 \\ &= -\frac{1}{2\Omega k_B T_n} \sum_{kk'} [1 - f^{(0)}(\mathbf{k})] f^{(0)}(\mathbf{k}') W_{kk'} \\ &\quad \times (1 + 2\alpha E_{\mathbf{k}'}) (k'_z - k_z)^2. \end{aligned} \quad (21)$$

The electron mobility follows from (18), (19) and $\sigma_n = e \mu_n n$

$$\mu_n = -\frac{en}{2\hbar^2 d_{00}}. \quad (22)$$

μ_n will be a function of the carrier temperature T_n via the heated Maxwellian, a function of the lattice temperature via the phonon occupation numbers, and a function of the doping concentration. To calculate μ_n , we have to choose a model for the band structure and to evaluate the six-fold integral $\sum_{kk'}$ for the relevant scattering mechanisms. In silicon the electrons populate six equivalent valleys. For very small $|\mathbf{k} - \mathbf{k}_0^{(v)}|$ the iso-energy surface of a valley v is a prolate ellipsoid of revolution with its center located at about $k_0^{(v)} \approx 0.85\pi/a$ in [100]-direction (a —lattice constant). With rising energy the band dispersion becomes nonparabolic. In first-order $k \cdot p$ -theory the nonparabolicity parameter α is independent of direction. Hence one can write

$$E_{\mathbf{k}}^{(v)}(\alpha E_{\mathbf{k}}^{(v)} + 1) = \frac{\hbar^2}{2} [(\mathbf{k} - \mathbf{k}_0^{(v)}), \hat{m}_{(v)}^{-1}(\mathbf{k} - \mathbf{k}_0^{(v)})]. \quad (23)$$

In order to be able to integrate analytically we use the spherical model

$$E_{\mathbf{k}}(\alpha E_{\mathbf{k}} + 1) = \frac{\hbar^2 k^2}{2m_{dn}}, \quad (24)$$

where m_{dn} denotes the DOS effective mass of one valley: $m_{dn} = (m_t^2 m_l)^{1/3}$. Then, the distribution function (2) is the same for all six valleys and summation over initial states

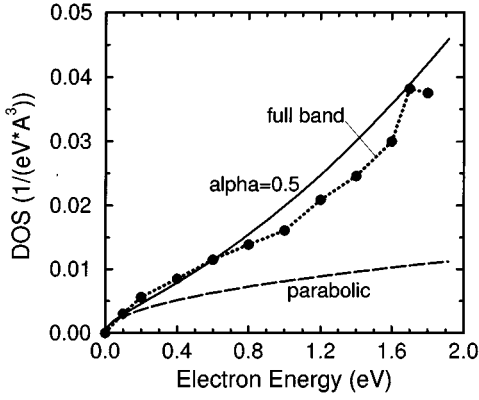


FIG. 2. Electron density of states $D_n(E)$ in silicon. The solid line represents the nonparabolic model (25) with DOS effective mass. The dotted line with circles is a pseudopotential full-band result used in MC simulation (see Ref. 9). The dashed curve is obtained setting $\alpha=0$ in (25).

\mathbf{k}' has to include a factor 6 to account for valley multiplicity. The spherical model (24) is in accordance with many HD transport models in silicon device simulation and also with earlier MC programs.^{3,10} On the other hand, there would be no essential improvement taking anisotropy into account, since the effective mass factors are multiplied by the deformation potential constants, the latter being fit parameters of the mobility model. For certain scattering mechanisms, as intravalley elastic ac-phonon scattering, the inverse RT is proportional to the DOS. Then, both (23) and (24) yield the same result. More generally, intravalley ac-phonon and intravalley scattering are randomizing in the sense of Herring and Vogt¹¹ making the scattering rates dependent on the DOS effective mass.¹²

Ionized impurity scattering is not randomizing; thus we will give the explicit expression of the partial mobility in the Born approximation using ellipsoidal energy surfaces (23). Comparison with the result based on the spherical model (24) will show that the anisotropy effect is at most 20%.

In contrast, nonparabolicity was found to be crucial, e.g., to reproduce drift velocity saturation. In Fig. 2 we compare the nonparabolic DOS model [resulting from Eq. (23)]

$$D_n(E) = \frac{2}{\sqrt{\pi}} \frac{N_c}{(kT_n)^{3/2}} \sqrt{E} \sqrt{\alpha E + 1} (2\alpha E + 1) \quad (25)$$

with the realistic DOS of a pseudopotential calculation.⁹ The nonparabolic model with $\alpha=0.5/\text{eV}$ is in reasonable agreement with the MC DOS up to $E=1$ eV.

It is worthwhile to shed some light on what distinguishes the variational method from the more familiar RTA. First of all, the latter is not strictly valid for a number of scattering mechanisms considered here: nonelastic acoustic-phonon scattering, nonpolar optical-phonon scattering (holes), and intervalley scattering (electrons). If, nevertheless, the RTA is applied to the linearized form of the BTE (1), it follows that

$$f^{(1)}(\mathbf{k}) = -\tau(E_{\mathbf{k}}) \left(\frac{\partial f^{(0)}}{\partial E_{\mathbf{k}}} \right) \mathbf{v}_g(\mathbf{k}) \cdot \mathbf{F}. \quad (26)$$

Inserting into (17) yields after short algebra

$$\mu_n = \frac{e}{3n} \int dE_{\mathbf{k}} D_n(E_{\mathbf{k}}) \left(-\frac{\partial f^{(0)}}{\partial E_{\mathbf{k}}} \right) \tau_n(E_{\mathbf{k}}) (\hbar^{-1} \nabla_{\mathbf{k}} E_{\mathbf{k}})^2, \quad (27)$$

which is the well-known result from linear response theory (see Refs. 13, 14, and 15, page 545). For a more direct comparison it is useful to consider the case of elastic ac-scattering, where a RT exists in rigor

$$\tau_{n,ac}^{-1}(E) = \frac{\pi D_{ac,n}^2 k_B T_L}{\hbar \rho c_l^2} D_n(E) \quad (28)$$

(for symbols see below). After inserting $\tau_{n,ac}$ into Eq. (27), $\mu_{n,ac}$ can be calculated exactly and then be compared with the result (44) of the variational method. One finds that the ratio is given by $\mu_{n,ac}^{Kohler} = (9\pi/32) \mu_{n,ac}^{RTA}$ which is the known failure of the Kohler method in first order ($\Phi(\mathbf{k}) = a_0 k_z$).¹⁶

For the goal of this work—the derivation of a closed-form expression that combines high- and low-field mobility—the RTA has still another drawback: even if approximate RTs would be used, the reciprocal summation rule to obtain the total RT finally would prevent an analytical integration.

B. Scattering mechanisms

1. Intravalley acoustic-phonon scattering

The transition probability for deformation potential coupling to longitudinal acoustic phonons reads

$$W_{\mathbf{k}'\mathbf{k}}^{ac} = \frac{\pi D_{ac,n}^2 q}{\Omega \rho c_l} \{ f_B(q) \delta_{\mathbf{k}-\mathbf{k}'+\mathbf{q},0} \delta(E_{\mathbf{k}'} - E_{\mathbf{k}} - \hbar c_l q) + [f_B(q) + 1] \delta_{\mathbf{k}-\mathbf{k}'-\mathbf{q},0} \delta(E_{\mathbf{k}'} - E_{\mathbf{k}} + \hbar c_l q) \}, \quad (29)$$

where $f_B(q) = \{ \exp[\hbar c_l q / (k_B T_L)] - 1 \}^{-1}$ denotes the phonon occupation number (Bose function). $D_{ac,n}$ is the deformation potential constant, ρ the mass density, and c_l the longitudinal sound velocity. The dispersion is taken into account by a linear, isotropic approximation $E_q = \hbar c_l q$. The contribution of transverse acoustic (TA) modes will be included in the final fit of the coupling constants.

2. Intervalley scattering

Intervalley scattering by optical and acoustic modes will be described neglecting phonon dispersion as well as the indirect, anisotropic band structure. The different contributions of optical and acoustic modes and the different deformation potential constants and phonon energies of f- and g-type processes will be lumped into a single effective deformation potential constant $D_{int,n}$ and a single effective phonon energy $\hbar \omega_{int,n}$. These parameters will be obtained by a proper root square sum of the various coupling constants used in first-principle MC simulations or by fitting the experimental mobility data. The simplified model for intervalley scattering then takes the form

$$W_{\mathbf{k}'\mathbf{k}}^{int} = \frac{\pi D_{int,n}^2}{\Omega \rho \omega_{int,n}} [f_B \delta(E_{\mathbf{k}'} - E_{\mathbf{k}} - \hbar \omega_{int,n}) + (f_B + 1) \delta(E_{\mathbf{k}'} - E_{\mathbf{k}} + \hbar \omega_{int,n})] \quad (30)$$

with $f_B = \{\exp[\hbar\omega_{int,n}/(k_B T_L)] - 1\}^{-1}$.

3. Impurity scattering

Scattering by ionized impurities will be considered only in Born approximation here. The Brooks-Herring theory, using a screened Coulomb potential, yields

$$W_{k'k}^{imp} = \frac{2\pi N_{imp}}{\hbar\Omega} \left(\frac{4\pi e^2 Z}{\epsilon_s} \right)^2 \frac{1}{(q^2 + \lambda_q^{-2})^2} \delta(E_{k'} - E_k). \quad (31)$$

N_{imp} denotes the total concentration of ionized dopants, Z is the charge number, ϵ_s the static dielectric constant, and λ_q^{-1} the screening length. The latter becomes a function of relative momentum q , if the polarization of the screening cloud is taken into account.¹⁷ This effect, as well as those related to the degeneracy of the electron gas, the non-spherical form of the valleys, and the perturbed DOS as result of heavy doping, will be addressed in Section II C 3.

C. Analytical results for the partial mobilities

According to Eq. (22) the mobility is determined by the quantity d_{00} defined in Eq. (21). We insert $W_{kk'} = W_{kk'}^{ac} + W_{kk'}^{int} + W_{kk'}^{imp}$ and use the abbreviation $(1 + 2\alpha E_k) = \gamma'(E_k)$, which is the derivative of

$$\gamma(E_k) = E_k(1 + \alpha E_k) \quad (32)$$

with respect to E_k . Collision integrals with Maxwellian distribution functions were calculated in the early days of semiconductor transport theory, mostly in connection with analytical solutions of the BTE.^{7,18-23} In this section we use the heated-Maxwellian approximation to evaluate the mobility in closed form (as function of lattice temperature, carrier temperature and doping), which goes beyond the calculation of the momentum relaxation time, since it requires additional integrations. Furthermore, nonparabolicity will be fully taken into account.

1. Non-elastic approach for intravalley acoustic-phonon scattering

Inserting the transition probability (29) into the expression for d_{00} Eq. (21) we find

$$\begin{aligned} d_{00}^{ac} = & - \frac{3\pi D_{ac,n}^2}{k_B T_n (8\pi^3)^2 \rho c_l} \int d^3 \mathbf{k} \int d^3 \mathbf{q} q^3 \cos^2 \Theta \\ & \times [1 - f^{(0)}(E_{|k+q|})] f^{(0)}(E_k) \gamma'(E_k) \{f_B(q) \delta(E_{|k+q|} \\ & - E_k - \hbar c_l q) + [f_B(q) + 1] \delta(E_{|k+q|} - E_k + \hbar c_l q)\}, \end{aligned} \quad (33)$$

where Θ denotes the angle between vector \mathbf{q} and z-axis. In the doping range where phonon scattering dominates the mobility, Boltzmann statistics can be applied and the factor $1 - f^{(0)}$ can be neglected. All angular integrations can be done exactly. The energy conservation δ -function yields upper and lower boundaries for the phonon wave vector \mathbf{q} as a function of electron momentum k . With the new variable $z = \hbar c_l q / (k_B T_L)$ we obtain

$$\begin{aligned} d_{00}^{ac} = & - \frac{D_{ac,n}^2 m_{dn}}{8 k_B T_n \hbar \pi^3 \rho} \left(\frac{k_B T_L}{\hbar c_l} \right)^6 \int_0^\infty dk k f^{(0)}(E_k) \\ & \times \left[\int_{z_{min}^a(k)}^{z_{max}^a(k)} dz \frac{z^4}{e^z - 1} \left(\frac{\gamma'(E_k)}{k_B T_L} + 2\alpha z \right) \right. \\ & \left. + \int_{z_{min}^e(k)}^{z_{max}^e(k)} dz \frac{z^4}{1 - e^{-z}} \left(\frac{\gamma'(E_k)}{k_B T_L} - 2\alpha z \right) \right]. \end{aligned} \quad (34)$$

The boundaries are given by

$$z_{min}^a(k) = \frac{4E_l}{k_B T_L} \frac{\gamma'(E_k)}{(1 - 4\alpha E_l)} \left(1 - \frac{v_g(k)}{c_l} \right) \Theta \left(1 - \frac{v_g(k)}{c_l} \right), \quad (35)$$

$$z_{max}^a(k) = \frac{4E_l}{k_B T_L} \frac{\gamma'(E_k)}{(1 - 4\alpha E_l)} \left(1 + \frac{v_g(k)}{c_l} \right), \quad (36)$$

$$z_{min}^e(k) = 0 \quad (37)$$

$$z_{max}^e(k) = \frac{4E_l}{k_B T_L} \frac{\gamma'(E_k)}{(1 - 4\alpha E_l)} \left(\frac{v_g(k)}{c_l} - 1 \right) \Theta \left(\frac{v_g(k)}{c_l} - 1 \right), \quad (38)$$

where $v_g(k) = \hbar k / (m_{dn} \gamma'(E_k))$ is the value of the group velocity, and for the LA-mode

$$E_l = \frac{m_{dn}}{2} c_l^2 = 2.3 \frac{m_{dn}}{m_0} \cdot 10^{-4} \text{ eV}. \quad (39)$$

If the group velocity is smaller than the sound velocity, the absorbed phonon cannot fall short of a certain value given by (35), and phonon emission is impossible at all due to the step function in (38). As can be seen from the Bose functions in (34), the upper limits are of the order $z = \hbar c_l 2k / (k_B T_L)$ ($2k$ is the diameter of the energy sphere). Inserting the value of c_l , this gives at room temperature: $z_{max} \approx 1.1 \sqrt{E}$ with E measured in eV. The equipartition approximation of the Bose distribution [$f_B(z) \approx 1/z$, $z \ll 1$] is therefore well justified, as long as the average electron energy does not exceed 0.2 eV. For an average energy up to 1 eV it is still an useful approximation which enables analytical z -integration. At even higher energies the validity of various assumptions made so far becomes questionable anyway. With the equipartition approximation the integral (34) turns into

$$\begin{aligned} d_{00}^{ac} = & - \frac{D_{ac,n}^2 n}{12 k_B T_n (2\pi)^3 \rho} \frac{m_{dn}^2 k_B T_L}{\hbar^4 c_l N_c} \int_0^\infty d\gamma e^{-\frac{\gamma}{k_B T_n}} \gamma' \\ & \times \left[\kappa_+^4(\gamma) \left(\frac{\gamma'}{\hbar c_l} + \frac{8\alpha}{5} \kappa_+(\gamma) \right) \right. \\ & \left. - \kappa_-^4(\gamma) \left(\frac{\gamma'}{\hbar c_l} + \frac{8\alpha}{5} \kappa_-(\gamma) \right) \Theta(\gamma_0 - \gamma) \right] \end{aligned} \quad (40)$$

with

$$\kappa_\pm(\gamma) = \frac{4\gamma_0}{\hbar c_l} \left(\gamma' \pm \sqrt{\frac{\gamma}{E_l}} \right) \quad (41)$$

$$\gamma_0 = \frac{E_l}{1 - 4\alpha E_l} \approx E_l. \quad (42)$$

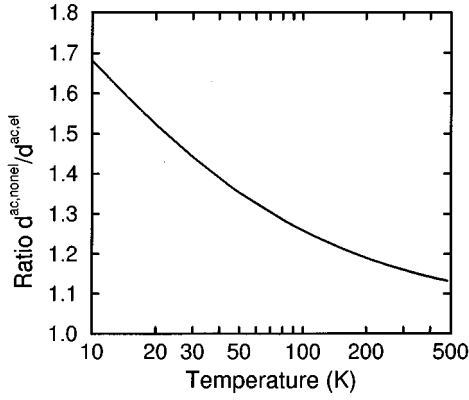


FIG. 3. Ratio of the scattering strengths of intravalley LA-phonon scattering calculated in elastic (44) and nonelastic approximation (46) for thermalized carriers ($T_n = T_L$). The temperature dependence of the DOS effective mass was taken into account by the relation $m_i(T_L)$ Eq. (96).

The elastic limit $E_l \rightarrow 0$, $\kappa_+ \rightarrow 2k$ enables also the last integration to be performed exactly, because

$$\begin{aligned} I_{ac}(T_n) &= \frac{1}{(k_B T_n)^3} \int_0^\infty d\gamma e^{-\frac{\gamma}{k_B T_n} \gamma'^2 \gamma^2} \\ &= \int_0^\infty dx e^{-x} x^2 (1 + 4\alpha k_B T_n x)^2 \\ &\equiv 2(1 + 12\tilde{\alpha}). \end{aligned} \quad (43)$$

The dimensionless nonparabolicity $\tilde{\alpha} = \alpha k_B T_n$ will be used in what follows. Thus, we obtain in the elastic approximation

$$d_{00}^{ac,el} = -\frac{4D_{ac,n}^2}{3(4\pi)^{3/2}} \left(\frac{2m_{dn}}{\hbar^2} \right)^{5/2} \frac{\sqrt{k_B T_n k_B T_L}}{\hbar \rho c_l^2} I_{ac}(T_n). \quad (44)$$

The nonelastic case can be solved approximately, making use of the small parameter

$$x_l = \frac{E_l}{k_B T_n}. \quad (45)$$

Eq. (39) shows that x_l remains small down to very low electron temperatures ($T_n \approx 10$ K). We only give the first-order correction here, which is sufficient even for 77 K application:

$$d_{00}^{ac,nonel} = d_{00}^{ac,el} \exp(-x_l) (1 + \sqrt{8x_l} \sqrt{1 + 8\tilde{\alpha}}). \quad (46)$$

Fig. 3 illustrates the nonelastic correction as a function of temperature assuming cold electrons. At room temperature the scattering strength is larger by about 16%, which increases to about 30% at 77 K, as compared to the elastic approximation.

2. Intervalley scattering

With the above mentioned assumptions, i.e., single effective phonon energy $\hbar \omega_{int,n}$ and single effective deformation potential constant of intervalley scattering $D_{int,n}$, and isotropic but nonparabolic valleys, one obtains the following exact expression for d_{00}^{int} :

$$d_{00}^{int} = -\frac{D_{int,n}^2 n}{3(4\pi)^{3/2}} \left(\frac{2m_{dn}}{\hbar^2} \right)^{5/2} \frac{\sqrt{k_B T_n}}{\rho \omega_{int,n}} f_B I_{int}(T_n, T_L), \quad (47)$$

with

$$\begin{aligned} f_B I_{int}(T_n, T_L) &= \int_0^\infty dx e^{-x} [f_B \sqrt{1 + 4\tilde{\alpha}x} + (f_B + 1)] e^{-2\xi(\sqrt{1 + 4\tilde{\alpha}x} + 2\tilde{\alpha}\xi)} \\ &\quad \times (\sqrt{1 + 4\tilde{\alpha}x} + 4\tilde{\alpha}\xi) (\sqrt{1 + 4\tilde{\alpha}x} + 4\tilde{\alpha}\xi) \\ &\quad \times [2x + 2\xi(\sqrt{1 + 4\tilde{\alpha}x} + 2\tilde{\alpha}\xi)] \\ &\quad \times \sqrt{x[x + 2\xi(\sqrt{1 + 4\tilde{\alpha}x} + 2\tilde{\alpha}\xi)]}. \end{aligned} \quad (48)$$

Here, the characteristic parameter is the dimensionless phonon energy

$$\xi = \frac{\hbar \omega_{int,n}}{2k_B T_n}. \quad (49)$$

If the carrier temperature is high enough that $\xi \ll 1$ holds, collisions are quasi-elastic and (48) turns into its high-temperature limit

$$f_B I_{int}^{el}(T_n, T_L) = 2(2f_B + 1) I_{ac}(T_n). \quad (50)$$

If the carriers are cold, nonparabolicity is of minor importance, and (48) can be evaluated with $\alpha = 0$ (parabolic approximation). This gives

$$\begin{aligned} f_B I_{int}^{par}(T_n, T_L) &= 2[f_B e^\xi + (f_B + 1)e^{-\xi}] \int_\xi^\infty dz e^{-z} z \sqrt{z^2 - \xi^2} \\ &= 2[f_B e^\xi + (f_B + 1)e^{-\xi}] \xi^2 K_2(\xi) \\ &= 2 \sinh^{-1}(\xi) \xi^2 K_2(\xi), \end{aligned} \quad (51)$$

where $K_2(\xi)$ denotes the modified Bessel function of second order.²⁴ Obviously, (50) and (51) can be combined to the final analytical form

$$f_B I_{int}(T_n, T_L) = \sinh^{-1}(\xi) \xi^2 K_2(\xi) I_{ac}(T_n). \quad (52)$$

The error of this approximation is about 3% almost independently of the electron temperature (see Fig. 4). At high carrier temperatures ($\xi \ll 1$) due to

$$\lim_{\xi \rightarrow 0} \xi^2 K_2(\xi) = 2 \quad (53)$$

this turns into

$$f_B I_{int}(T_n \rightarrow \infty, T_L) = 2(2f_B + 1) I_{ac}(T_n). \quad (54)$$

3. Impurity scattering including dispersive screening

Isotropic valley: We first consider isotropic valleys. Inserting (31) into the expression for d_{00} we obtain

$$\begin{aligned} d_{00}^{imp} &= -\frac{4N_{imp} m_{dn}^2 e^4 Z^2}{\hbar^5 \pi k_B T_n \epsilon_s^2} \int_0^\infty d\gamma \gamma'^2 f^{(0)}(\gamma) \\ &\quad \times [1 - f^{(0)}(\gamma)] \int_{q_{min}}^{q_{max}} dq \frac{q^3}{[q^2 + L_D^{-2} J(q, \alpha)]^2} \end{aligned} \quad (55)$$

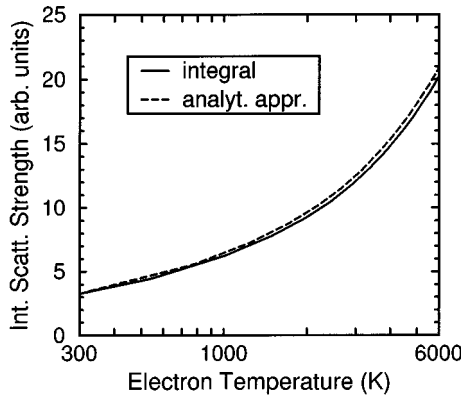


FIG. 4. Intervalley scattering strength as a function of carrier temperature. Solid line: numerical integral (48), dashed line: analytical approximation (52).

with

$$q_{min}=0, \quad q_{max}=2\sqrt{\frac{2m_{dn}\gamma}{\hbar^2}}. \quad (56)$$

In Eq. (55) L_D denotes the Debye screening length, which in the Thomas-Fermi approximation is calculated by the formula (contribution of holes and ionized impurities to screening neglected here for simplicity)

$$L_D^{-2} = \frac{4\pi e^2 Z}{\epsilon_s k_B T_n} \frac{\partial n}{\partial \eta_n}. \quad (57)$$

The factor $J(q, \alpha)$ accounts for both the dispersive screening and the effect of nonparabolicity on screening. Analytical expressions will be derived below. There it will be shown that $J(q, \alpha)$ is a slowly varying function of q around \hat{q} , the momentum for which the q -integrand in (55) becomes maximum. This momentum \hat{q} can be determined approximately setting $J(q, \alpha) \approx J(0, 0) = 1$, the limit of q -independent screening and parabolic bands. Then,

$$\hat{q} = \sqrt{3}L_D^{-1}. \quad (58)$$

With frozen $J(\hat{q}, \alpha)$ the q -integral in (55) is straightforward and we obtain

$$d_{00}^{imp} = -\frac{2N_{imp}m_{dn}^2 e^4 Z^2}{\hbar^5 \pi \epsilon_s^2} I_{imp}(a_n) \quad (59)$$

with

$$I_{imp}(a_n) = a_n \int_0^\infty dx (1 + 4\tilde{\alpha}a_n x) f^{(0)}(x) [1 - f^{(0)}(x)] \times \left[\ln(1+x) - \frac{x}{1+x} \right], \quad (60)$$

the Fermi function $f^{(0)}(x) = [\exp(a_n x - \eta_n) + 1]^{-1}$, and the screening parameter a_n

$$a_n = \frac{\hbar^2 L_D^{-2} J(\hat{q}, \alpha)}{8m_{dn} k_B T_n}. \quad (61)$$

The integral (60) can be solved exactly in the two cases of nondegenerate and completely degenerate statistics, respectively. In the first case $f^{(0)}(x) \rightarrow \exp(\eta_n - a_n x)$, and

$$I_{imp}^{dg}(a_n) = \frac{n}{N_c} \{ [(a_n + 1)E_1(a_n)e^{a_n} - 1](1 - 4\tilde{\alpha}a_n) + 4\tilde{\alpha}E_1(a_n)e^{a_n} \}, \quad (62)$$

where E_1 is the exponential integral function.²⁴ In the second case $f^{(0)}(x) \rightarrow \Theta(\eta_n - a_n x)$. Assuming still that the DOS is ideal, i.e., Eq. (25) holds, it follows that

$$I_{imp}^{dg}(a_n) = \left[\ln\left(1 + \frac{\eta_n}{a_n}\right) - \frac{\eta_n}{a_n + \eta_n} \right] (1 + 4\tilde{\alpha}\eta_n). \quad (63)$$

The assumption of an unperturbed DOS in the heavy doping regime is not well justified as will be shown below. In (60)–(63) the screening parameter a_n and the normalized Fermi level η_n are functions of the carrier density. If degenerate statistics has to be applied, Fermi level and density are related by the Fermi integral $F_{1/2}$, again under the assumption of an unperturbed DOS. With a model for the perturbed DOS the $\eta_n(n)$ -relation becomes extremely complicated, since the screening length itself is the parameter of the DOS model.

For the moment we assume an ideal DOS given by Eq. (25) over the entire doping range. For the purpose of device simulation an analytical $\eta_n(n)$ -relation is desirable to enable fast computation of the screening parameter and the scattering integral I_{imp} . It is important to note that due to the choice of the distribution function $f^{(0)}(\mathbf{k})$ Eq. (5) the electron density is indeed given by the usual Fermi integral ($n = N_c F_{1/2}$) and not by its nonparabolic modification ($n = N_c J_{1/2}$), discussed, e.g., in Ref. 16. This can be easily proven evaluating the zeroth moment of $f^{(0)}(\mathbf{k})$. The screening length is determined by the Fermi integral $F_{-1/2}$. We adopt the approximation given in Ref. 25 (corrected for typographical errors and slightly improved in accuracy)

$$\frac{\partial n}{\partial \eta_n} \approx \frac{\Theta\left(5.97455 - \frac{n}{N_c}\right)n}{1 + 0.3536\frac{n}{N_c} - 0.0099\left(\frac{n}{N_c}\right)^2 + 0.000375\left(\frac{n}{N_c}\right)^3} + \frac{1.5\Theta\left(\frac{n}{N_c} - 5.97455\right)N_c\left(\frac{n}{N_c}\right)^{1/3}}{1.209 + 0.6803\left(\frac{n}{N_c}\right)^{-4/3} + 2.55\left(\frac{n}{N_c}\right)^{-8/3}}. \quad (64)$$

The Fermi level η_n is determined by the inverse function of the Fermi integral. The approximation analogous to (64) reads²⁵

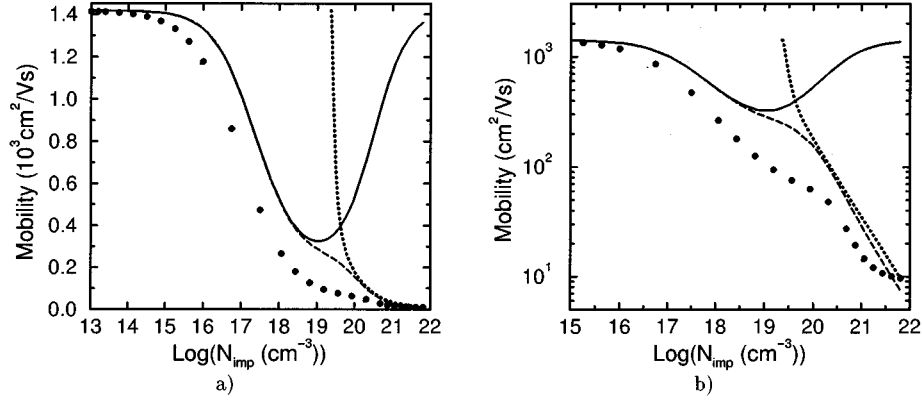


FIG. 5. Calculated mobility as function of doping. (a) Log-lin plot; (b) Log-log plot. Parameters: $T_n = T_L = 300$ K, $\alpha = 0.5/eV$. Solid curve: with I_{imp}^{ndg} Eq. (62) and Boltzmann statistics in the screening parameter; dashed curve: with I_{imp}^{ndg} Eq. (62) but correct screening [Eqs. (64) and (65)]; dotted curve: with I_{imp}^{dg} Eq. (63) but correct screening [Eqs. (64) and (65)]; filled circles: experimental data (see Ref. 26).

$$\begin{aligned} \eta_n \approx & \Theta \left(5.97455 - \frac{n}{N_c} \right) \left[\ln \left(\frac{n}{N_c} \right) + 0.3536 \left(\frac{n}{N_c} \right) \right. \\ & - 0.00459 \left(\frac{n}{N_c} \right)^2 + 0.000125 \left(\frac{n}{N_c} \right)^3 \left. \right] \\ & + \Theta \left(\frac{n}{N_c} - 5.97455 \right) \left[1.209 \left(\frac{n}{N_c} \right)^{2/3} \right. \\ & \left. - 0.6803 \left(\frac{n}{N_c} \right)^{-2/3} - 0.85 \left(\frac{n}{N_c} \right)^{-2} \right]. \end{aligned} \quad (65)$$

In Fig. 5 we compare the calculated mobility curves as function of the concentration of ionized impurities (assuming neutrality, i.e., $n = N_{imp}$) against experimental data.²⁶ The effect of dispersive screening was not included, and the DOS was assumed to be ideal even at the highest densities. The theoretical mobility comes out too large for all doping levels, and exhibits a particularly strong deviation in the range $10^{19} \text{ cm}^{-3} - 10^{20} \text{ cm}^{-3}$. Furthermore, calculating the screening parameter with Boltzmann statistics yields completely unphysical results (i.e., an increase in μ with doping) for carrier densities beyond 10^{19} cm^{-3} . Fortunately, if I_{imp}^{ndg} with the correct screening is used, the result differs only little from the exact one obtained by evaluating the integral I_{imp} Eq. (60) numerically. This is illustrated in Fig. 6.

Anisotropic Valley: The influence of the ellipsoidal energy surface on the partial mobility $\mu_{imp} = -en/(2\hbar^2 d_{00}^{imp})$ will be studied for the two valleys along [001]- and [100]-direction, respectively. The rotational axes of these valleys are parallel and orthogonal to the applied electric field (z -direction), respectively. In the first case we can still take advantage of the cylindrical symmetry and carry out the polar \mathbf{q} -integration exactly, whereas in the latter case the approximation $\sin^2 \varphi \approx \cos^2 \varphi \approx 1/2$ must be used. The result is

$$d_{00,j}^{imp} = - \frac{N_{imp} m_{dn}^2 e^4 Z^2}{\hbar^5 \pi \epsilon_s^2} \int_0^1 d\tau \tau^2 \frac{m_j m_{dn}}{\mu_j^2(\tau)} I_{imp} \left(a_n \frac{m_{dn}}{\mu_j(\tau)} \right), \quad (66)$$

where the index j equals either l (longitudinal) or t (transverse) and I_{imp} is a function of τ . The mass $\mu_j(\tau)$ is defined by

$$\mu_l(\tau) = \tau^2(m_l - m_t) + m_t, \quad (67)$$

$$\mu_t(\tau) = -\frac{1}{2}[\tau^2(m_l - m_t) - (m_l + m_t)]. \quad (68)$$

For clarity we rewrite (66):

$$\begin{aligned} d_{00,l}^{imp} = & - \frac{N_{imp} m_{dn}^2 e^4 Z^2}{\hbar^5 \pi \epsilon_s^2} \frac{m_l}{2(m_l - m_t)^{3/2}} \\ & \times \int_{m_{dn}/m_l}^{m_{dn}/m_t} dy \sqrt{m_{dn}/y - m_t} I_{imp}(y a_n), \end{aligned} \quad (69)$$

$$\begin{aligned} d_{00,t}^{imp} = & - \frac{N_{imp} m_{dn}^2 e^4 Z^2}{\hbar^5 \pi \epsilon_s^2} \frac{\sqrt{2} m_t}{(m_l - m_t)^{3/2}} \\ & \times \int_{2m_{dn}/(m_l + m_t)}^{m_{dn}/m_t} dy \sqrt{(m_l + m_t)/2 - m_{dn}/y} I_{imp}(y a_n). \end{aligned} \quad (70)$$

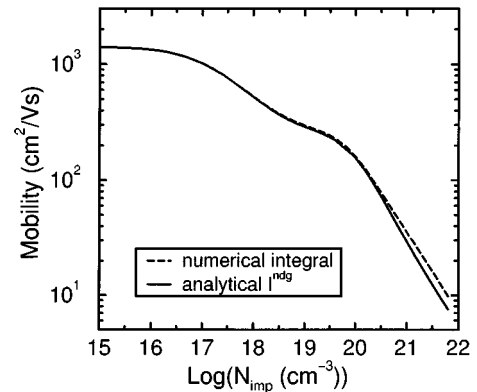


FIG. 6. Mobility calculated with I_{imp}^{ndg} Eq. (62) (solid line) and the numerical integral Eq. (60) (dashed line). Parameters: $T_n = T_L = 300$ K, $\alpha = 0.5/eV$.

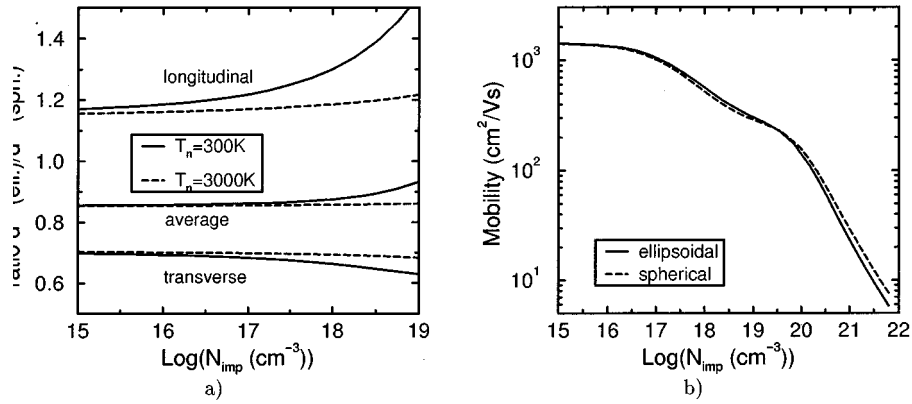


FIG. 7. (a) Ratio of the scattering integrals $d_{00,l}^{imp}/d_{00}^{imp}$ (longitudinal), $d_{00,t}^{imp}/d_{00}^{imp}$ (transverse), and $(d_{00,l}^{imp} + 2 d_{00,t}^{imp})/(3 d_{00}^{imp})$ (average). (b) Anisotropy effect on mobility as function of carrier density. Parameters: $T_n = T_L = 300$ K, $\alpha = 0.5/\text{eV}$. Solid curve: with $(d_{00,l}^{imp} + 2 d_{00,t}^{imp})/3$ [Eqs. (69) and (70)]; dashed curve: with d_{00}^{imp} [Eq. (59)]. In both cases the analytical form (60) was used for I_{imp} .

From (66)–(70) it turns out that the isotropic scattering integral is averaged over the effective mass in the screening length with an anisotropic weight function. For the two longitudinal valleys the mass varies between the extremes m_l and m_t , whereas for the four transverse valleys the variation is between the mean value $(m_l + m_t)/2$ and m_t . There is no analytical approach for the integrals in (69) and (70). In Fig. 7 the numerical evaluation is shown in terms of the ratio between the scattering strengths in ellipsoidal and spherical valleys. When anisotropy is taken into account, the scattering strength increases in the longitudinal valleys, whereas it decreases in the transverse valleys. This can be understood from the weight functions in Eqs. (69) and (70): in the longitudinal valley the “integral” effective mass is larger than the DOS mass, which makes screening less efficient. At the same time, the “integral” DOS prefactor increases. The opposite holds for the transverse valleys. The total mobility is determined by the average $(d_{00,l}^{imp} + 2 d_{00,t}^{imp})/3$. Compared to the isotropic case, this average is smaller by about 15% in the low doping range. Thus, all six valleys together yield a rather small anisotropy effect. Decreasing carrier temperature and rising doping level intensify the effect as shown in Fig. 7. We note that the above results are in qualitative agreement with those of Refs. 27, 28 where the momentum relaxation time in the diffusion approximation and in the regime of Ohm’s law was calculated including anisotropic scattering by ionized impurities.

Dispersive Screening: The correct description of screening is crucial, if one aims at a good agreement between the calculated and measured mobilities in the range of moderate and heavy doping. We use the model distribution function (5) in order to derive an analytical expression for the factor $J(q, \alpha)$ which appears in Eq. (61) for the screening parameter. This extends the treatment given by Takimoto¹⁷ to Fermi statistics and nonparabolic bands. Our starting point is the dielectric function in the random phase approximation (RPA) (see e.g., Ref. 29, p.158) restricted to the lowest conduction band

$$\epsilon(\mathbf{q}) = 1 - \frac{e^2}{q^2 \pi^2 \epsilon_s} \int d^3k f^{(0)}(\mathbf{k}) \left(\frac{1}{E_{\mathbf{k}} - E_{\mathbf{k}-\mathbf{q}}} - \frac{1}{E_{\mathbf{k}+\mathbf{q}} - E_{\mathbf{k}}} \right). \quad (71)$$

First, we consider non-degenerate statistics. Inserting the heated Maxwellian (2) into Eq. (71) gives:

$$\epsilon(\mathbf{q}) = 1 + \frac{\tilde{\alpha}}{L_D^2 q^2} \frac{1}{\zeta \sqrt{\pi}} \int_0^\infty dx x e^{-x^2} \int_{-4\zeta x}^{4\zeta x} dz \times \left(\frac{1}{\sqrt{1 + 4\tilde{\alpha}x^2} - \sqrt{1 + 4\tilde{\alpha}(x^2 + 4\zeta^2)} - 4\tilde{\alpha}\zeta} + \frac{1}{\sqrt{1 + 4\tilde{\alpha}x^2} - \sqrt{1 + 4\tilde{\alpha}(x^2 + 4\zeta^2)} + 4\tilde{\alpha}\zeta} \right), \quad (72)$$

with

$$\zeta = \zeta(q) = \frac{\hbar q}{\sqrt{8m_{dn}k_B T_n}}. \quad (73)$$

The integral in z can be solved exactly. As in the case of parabolic bands¹⁷ it remains one integration which cannot be performed analytically:

$$\epsilon(q) = 1 + \frac{1}{q^2 L_D^2} J(\zeta, \tilde{\alpha}), \quad (74)$$

where

$$J(\zeta, \tilde{\alpha}) = \frac{1}{\sqrt{\pi}\zeta} \int_0^\infty dx x e^{-x^2} \left(\sqrt{1 + 4\tilde{\alpha}(x + 2\zeta)^2} - \sqrt{1 + 4\tilde{\alpha}(x - 2\zeta)^2} + \sqrt{1 + 4\tilde{\alpha}x^2} \ln \left| \frac{\sqrt{1 + 4\tilde{\alpha}(x + 2\zeta)^2} - \sqrt{1 + 4\tilde{\alpha}x^2}}{\sqrt{1 + 4\tilde{\alpha}(x - 2\zeta)^2} - \sqrt{1 + 4\tilde{\alpha}x^2}} \right| \right). \quad (75)$$

In order to avoid the numerical evaluation of $J(\zeta, \tilde{\alpha})$ we look for an analytical interpolation between the limits $\zeta \rightarrow 0$ and $\zeta \rightarrow \infty$. In the first case one obtains

$$J(0, \tilde{\alpha}) = \frac{2}{\sqrt{\pi}} \int_0^\infty dx e^{-x^2} \frac{(1 + 8\tilde{\alpha}x^2)}{\sqrt{1 + 4\tilde{\alpha}x^2}} \approx \sqrt{1 + 6\tilde{\alpha} - 2\tilde{\alpha}^2}. \quad (76)$$

The last approximation is satisfactory up to electron temperatures of $T_n \approx 10\,000$ K. In the second case one obtains

$$\begin{aligned} J(\infty, \tilde{\alpha}) &= \frac{\sqrt{\tilde{\alpha}}}{\zeta} + \frac{1}{\sqrt{\pi}\zeta^2} \int_0^\infty dx x^2 e^{-x^2} \sqrt{1 + 4\tilde{\alpha}x^2} \\ &\approx \frac{\sqrt{\tilde{\alpha}}}{\zeta} + \frac{\sqrt{1 + 4\tilde{\alpha}}}{4\zeta^2} \quad (\tilde{\alpha} \neq 0). \end{aligned} \quad (77)$$

A good fit to $J(\zeta, \tilde{\alpha})$ for all ζ and $\tilde{\alpha}$ is provided by the expression

$$\begin{aligned} J(\zeta, \tilde{\alpha}) &\approx \frac{J(0, \tilde{\alpha})}{2} \left\{ \left(1 + \frac{2}{3}\zeta^4 \right)^{-1} \right. \\ &\quad \left. + \left[1 + \frac{1}{2} \frac{J(0, \tilde{\alpha})}{J(\infty, \tilde{\alpha})} \right]^{-1} \right\}. \end{aligned} \quad (78)$$

Fig. 8 compares this approximation with the numerical integral (75) for different carrier temperatures. With rising T_n the $J(q, \tilde{\alpha})$ -factor increases at each q , indicating that screening is enhanced as the electrons become more energetic.

The main contributions to the mobility come from q -values of the order $\sqrt{3}L_D^{-1}$ [see Eq. (58)]. Therefore, the dominant wave numbers increase with rising carrier density. From a certain density ($\approx 10^{18} \text{ cm}^{-3}$) on, the screening parameter is reduced and the mobility drops. Since densities beyond 10^{19} cm^{-3} require Fermi statistics, we still need the expression of $J(\zeta, \tilde{\alpha})$ for this case. It can be shown that (78) may be used in this case as well, the only difference being that $J(0, \tilde{\alpha})$ has to be replaced by

$$J(0, \tilde{\alpha}, \eta_n) \approx \left(\frac{F_{-1/2}(\eta_n)}{F_{1/2}(\eta_n)} + 6\tilde{\alpha} - 2\tilde{\alpha}^2 \frac{F_{3/2}(\eta_n)}{F_{1/2}(\eta_n)} \right)^{1/2}. \quad (79)$$

The effect of dispersive screening on the mobility is illustrated in Fig. 9. It causes a drop in the mobility for densities greater than about 10^{18} cm^{-3} . If I_{imp}^{ndg} Eq. (62) is used, the mobility becomes too low and the error in the range $n > 10^{20} \text{ cm}^{-3}$ increases (dashed curve). With the numerical integral of Eq. (60) (solid curve), the fit improves.

Effect of Perturbed DOS: If the doping concentration exceeds a certain level, the silicon DOS changes near the band edge of majority carriers. We adopt the models proposed by Kane³⁰ and Morgan³¹ for the tail states and the impurity bands, respectively, to study the effect of a perturbed DOS on mobility. It turns out that—again—the largest effect is on the screening parameter, whereas the scattering integral I_{imp} remains almost unchanged, except for very low temperatures and extremely high doping ($N_{imp} > 10^{20} \text{ cm}^{-3}$). Energy levels of the order $\sim k_B T_n$ measured from the unperturbed DOS edge, which yield the major contribution to the mobility, are still well separated from the impurity

band for concentrations $N_{imp} < N_c$. As N_{imp} increases further, the DOS near the original DOS edge becomes completely extrinsic and the results will depend solely on the DOS model and its parameters. A quantitative analysis of the mobility in the ultra-heavy doping range is further complicated by the breakdown of the Born approximation and possible clustering of impurity atoms.

The DOS effect on the screening length is more pronounced, since $a_n \sim \partial n / \partial \eta_n$ is sensitive to the shape of the DOS edge when the Fermi level approaches it. We use the envelope of Kane's tail state model and Morgan's impurity band model (see Ref. 32 and references therein), and evaluate the electron density by

$$n = \int_{-E_g/2}^\infty dE f^{(0)}(E) \max[D_c(E), D_{ib}(E)], \quad (80)$$

with the conduction band DOS model $D_c(E)$ including tail states,³⁰ and the impurity band DOS model $D_{ib}(E)$ ³¹ described by

$$D_c(E) = \frac{2N_c}{\sqrt{\pi}(k_B T_n)^{3/2}} \sqrt{\sigma_{cv}} Y\left(\frac{E - E_c}{\sigma_{cv}}\right), \quad (81)$$

$$D_{ib}(E) = \frac{2N_D^+}{\sqrt{\pi}\sigma_{DA}} \exp\left(-\frac{(E - E_D)^2}{\sigma_{DA}^2}\right). \quad (82)$$

In these models the standard deviations have the form

$$\sigma_{cv} = \frac{q^2}{\sqrt{4\pi\epsilon_s}} \sqrt{(N_D^+ + N_A^-)\lambda} \exp\left(-\frac{a}{2\lambda}\right) \quad (83)$$

$$\sigma_{DA} = 1.0344\sigma_{cv} \exp\left(-\frac{1}{\sqrt{11.3206\pi(N_D^+ + N_A^-)\lambda^3}}\right). \quad (84)$$

The function Y is defined by

$$Y(x) = \frac{1}{\sqrt{\pi}} \int_{-\infty}^x du e^{-u^2} \sqrt{x - u}, \quad (85)$$

a denotes the lattice constant and λ the screening length. The screening length is a function of the DOS, hence Eqs. (81) and (82) represent a problem to be solved self-consistently. Here we restrict ourselves to the zeroth order solution with $\lambda = L_D$ and L_D calculated with the ideal DOS (25). The shape of the total DOS is sensitive to the dependence of the binding energy E_D of the donor electron on the doping concentration. This dependence primarily determines the screening parameter a_n in the heavy doping range. Following Refs. 33 and 34 we assume that

$$E_D(N_D^+) = E_D(0) - 3.1 \times 10^{-8} (N_D^+)^{1/3}. \quad (86)$$

The resulting DOS is illustrated in Fig. 10. The effect of the perturbed DOS on the mobility is illustrated in Fig. 11. If the model (81)–(86) is applied only to the screening parameter a_n , the mobility increases in the heavy doping range $N_{imp} > 10^{20} \text{ cm}^{-3}$ (solid curve). A further strong increase of the mobility for densities larger than 10^{19} cm^{-3} results, if the scattering integral (60) is evaluated numerically, with the model (81)–(86) also applied to the DOS factor in I_{imp} (dot-

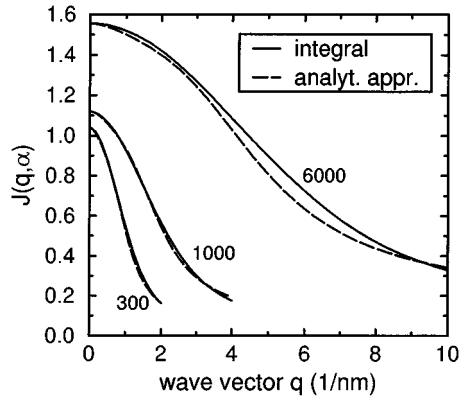


FIG. 8. Comparison of the analytical approximation for $J(q, \tilde{\alpha})$ given by Eq. (78) (dashed curves) and the numerical integral Eq. (75) (solid curves) for three different carrier temperatures. Parameters: $T_L=300$ K, $\alpha=0.5/\text{eV}$.

dashed curve). The mobility edge which separates localized electronic states below from extended states above (see Ref. 15, page 932), was assumed to coincide with the former band edge. Since the DOS becomes extrinsic near the band edge for $N_{imp} \approx 10^{19} \text{ cm}^{-3}$, the Fermi level at a given carrier density is lower than in the case of an ideal DOS. As a consequence, the contribution from the distribution function to the scattering integral (60) decreases, and the mobility increases. This is partly compensated by the growing scattering strength due to the DOS factor in I_{imp} . The combined action of these two effects yields the shoulder in the mobility curve around $N_{imp} = 10^{20} \text{ cm}^{-3}$. A similar shoulder appears in the experimental data. The subsequent drop (“second drop”) of the mobility is sometimes attributed to clustering of impurity atoms.³⁵

The major conclusion of this paragraph is that the real DOS has a strong impact on the mobility of silicon for doping concentrations larger than 10^{19} cm^{-3} . Theoretical results depend on the model assumptions and the computation time

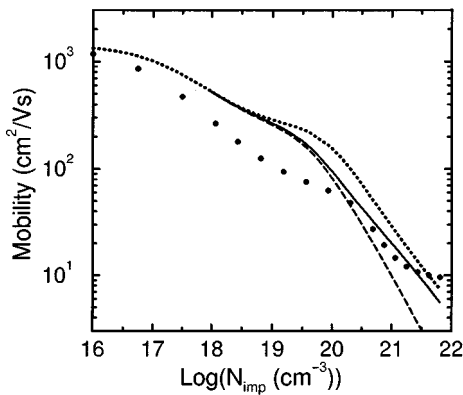


FIG. 9. Effect of dispersive screening on the mobility. Dotted curve: without dispersive screening and with I_{imp}^{ndg} [Eq. (62)]; dashed curve: with dispersive screening and I_{imp}^{ndg} [Eq. (62)]; solid curve: with dispersive screening and the numerical integral (60); filled circles: experimental data (see Ref. 26). Parameters: $T_n=T_L=300$ K, $\alpha=0.5/\text{eV}$.

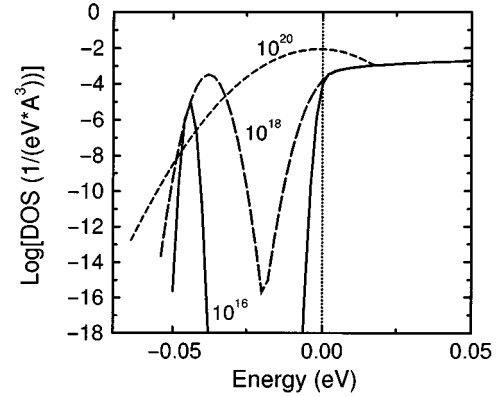


FIG. 10. Calculated total DOS according to (81), (82), and (86) for donors with $E_D(0)=0.045$ eV.

strongly increases. The latter fact makes the inclusion of real-DOS effects in device simulation codes impractical.

III. PARAMETER FIT AND COMPARISON WITH EXPERIMENTAL DATA

A. Fit procedure

The final form of the mobility model is:

$$\mu_n(T_L, T_n, N_{imp}) = \frac{\mu_n^{(0)}(T_L)}{f_{ac}(T_L, T_n) + f_{int}(T_L, T_n) + f_{imp}(T_L, T_n, N_{imp})}, \quad (87)$$

with a “scaling” mobility

$$\mu_n^{(0)}(T_L) = \frac{9 e \hbar}{m_{dn} k_B T_L} = 457.2 \left(\frac{300}{T_L} \right) \left(\frac{m_0}{m_{dn}} \right) \frac{\text{cm}^2}{\text{Vs}}, \quad (88)$$

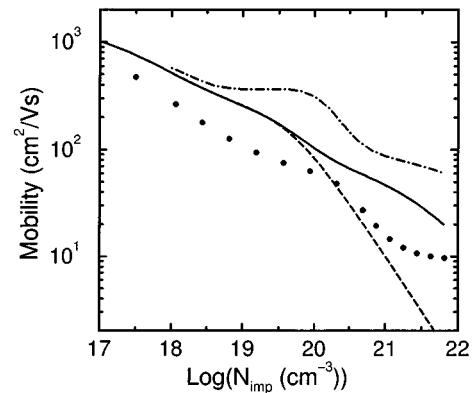


FIG. 11. Effect of perturbed DOS on the mobility calculated with dispersive screening. Dashed curve: with ideal DOS and I_{imp}^{ndg} [Eq. (62)]; solid curve: only screening parameter calculated with perturbed-DOS model (81)–(86), scattering integral I_{imp}^{ndg} [Eq. (62)]; dot-dashed curve: full numerical integration with perturbed-DOS model (81)–(86) including self-consistent calculation of the Fermi level and introducing the DOS model for the density of states in the scattering integral I_{imp} ; filled circles: experimental data (see Ref. 26). Parameters: $T_n=T_L=300$ K, $\alpha=0.5/\text{eV}$, $\lambda=L_D$, $E_D=0.045$ eV.

which happens to give the right order of magnitude (1357 cm²/Vs at room temperature). Recalling Eqs. (22), (43), (44), (46), (47), (52), (59), (61), and (62), the terms in the denominator can be expressed as

$$f_{ac} = \frac{48m_{dn}^{5/2}}{(2\pi)^{3/2}\hbar^3} \frac{(1+12\tilde{\alpha})}{\rho\sqrt{k_B T_n}} \sum_{j=LA,TA} \frac{D_j^2}{x_j} e^{-x_j} \times (1 + \sqrt{8x_j}\sqrt{1+8\tilde{\alpha}}) \quad (89)$$

$$= 3.53 \times 10^{-4} \left(\frac{m_{dn}}{m_0}\right)^{5/2} \sqrt{\frac{300}{T_n}} \times (1+12\tilde{\alpha}) \sum_{j=LA,TA} \frac{D_j^2}{x_j} e^{-x_j} \times (1 + \sqrt{8x_j}\sqrt{1+8\tilde{\alpha}}), \quad (90)$$

$$f_{int} = \frac{24}{(4\pi)^{3/2}} \left(\frac{2m_{dn}}{\hbar^2}\right)^{3/2} \frac{\sqrt{k_B T_n} \hbar D_{int,n}^2}{k_B T_L \rho \omega_{int,n}} \times (1+12\tilde{\alpha}) \sinh^{-1}(\xi) \xi^2 K_2(\xi) \quad (91)$$

$$= 1.34 \times 10^{-19} \frac{D_{int,n}^2}{\hbar \omega_{int,n}} \sqrt{\frac{T_n}{300}} \left(\frac{m_{dn}}{m_0}\right)^{3/2} \left(\frac{300}{T_L}\right) \times (1+12\tilde{\alpha}) \sinh^{-1}(\xi) \xi^2 K_2(\xi), \quad (92)$$

$$f_{imp} = 12 \sqrt{\frac{\hbar^2}{2m_{dn}}} \left(\frac{e^2 Z}{\epsilon_s}\right)^2 \frac{\sqrt{\pi} N_{imp}}{k_B T_L (k_B T_n)^{3/2}} \times \{[(a_n+1)E_1(a_n)e^{a_n}-1](1-4\tilde{\alpha}a_n) + 4\tilde{\alpha}E_1(a_n)e^{a_n}\} \quad (93)$$

$$= 5.88 \times 10^{-19} N_{imp} \sqrt{\frac{m_0}{m_{dn}}} \left(\frac{300}{T_n}\right)^{3/2} \left(\frac{300}{T_L}\right) \times \{[(a_n+1)E_1(a_n)e^{a_n}-1](1-4\tilde{\alpha}a_n) + 4\tilde{\alpha}E_1(a_n)e^{a_n}\}, \quad (94)$$

where

$$x_j = \frac{m_{dn} c_j^2}{2k_B T_n}, \quad \xi = \frac{\hbar \omega_{int,n}}{2k_B T_n}, \quad \tilde{\alpha} = \alpha k_B T_n. \quad (95)$$

The following parameters are regarded as given quantities: the nonparabolicity $\alpha = 0.5/\text{eV}$, the mass density $\rho = 2.329 \text{ g/cm}^3$, the charge number $Z = 1$, the static dielectric constant $\epsilon_s = 11.7$, and the DOS effective mass $m_{dn} = [m_t^2(T_L)m_l]^{1/3}$ with $m_l = 0.9163m_0$. The transverse effective mass m_t is a function of lattice temperature. We adopt the relation given in Ref. 36

$$m_t(T_L) = 0.1905m_0 \frac{1.206}{1.206 - 2.73 \times 10^{-4} T_L}. \quad (96)$$

Intravalley acoustic phonon scattering was generalized to both the LA branch and the degenerate TA branch: the sound velocities are $c_{LA} = 9.04 \times 10^5 \text{ cm/s}$ and $c_{TA} = 6.22 \times 10^5 \text{ cm/s}$, respectively.

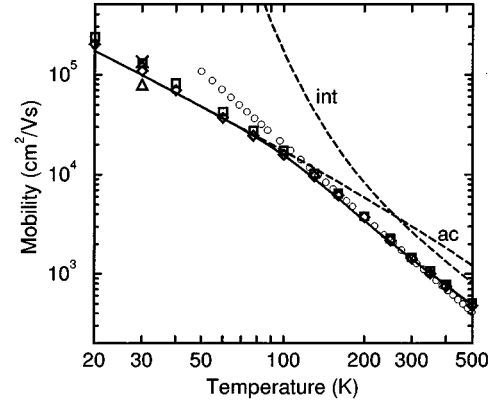


FIG. 12. Electron mobility as a function of lattice temperature (thermalized carriers assumed). Solid line: model of the present paper; dashed lines: contributions of acoustic phonon intravalley (ac) and intervalley scattering (int), resp.; circles: the power law of Ref. 41; diamonds: exp. data of Ref. 28; squares: exp. data of Ref. 38; \times : exp. point of Ref. 39; triangle: exp. point of Ref. 40.

The corresponding deformation potentials D_{LA} , D_{TA} have to be specified. For intervalley scattering the effective deformation potential constant $D_{int,n}$ and the effective phonon energy $\hbar \omega_{int,n}$ are needed. Furthermore, we allow for a scaling factor in f_{imp} to improve the fit where the mobility is dominated by impurity scattering. Together these are five fit parameters, which have been determined by comparison with first-principle MC results³⁷ and experimental data. The fit procedure is as follows: first, the acoustic deformation potentials D_{LA} and D_{TA} are fixed to the values based on empirical-pseudopotential calculations and properly adjusted in the MC code of Ref. 37: $D_{LA} = 5.49 \text{ eV}$, $D_{TA} = 2.58 \text{ eV}$. Second, $D_{int,n}$ is estimated by a root square sum over all individual intervalley deformation potentials used in Ref. 9. Then, $\hbar \omega_{int,n}$ is adjusted to reproduce the value of the lattice mobility at room temperature. As will be shown below, both the experimentally observed dependence of the mobility on a broad range of lattice temperatures and the saturation of drift velocity (dependence on carrier temperature) are recovered. Finally, the scaling factor in f_{imp} is found for a reasonable fit of the mobility as a function of doping concentration.

B. Dependence on ambient temperature

The lattice mobility at room temperature²⁶ is reproduced with $D_{int,n} = 6.68 \times 10^8 \text{ eV/cm}$ and $\hbar \omega_{int,n} = 0.0454 \text{ eV}$. The effective deformation potential constant was calculated by the root square sum

$$D_{int,n} = \sqrt{\sum_i D_i^2}, \quad (97)$$

with all X-X-valley f- and g-type and X-L-valley deformation potentials D_i from Ref. 9. The value of $\hbar \omega_{int,n}$ is considerably smaller than the LO-phonon energy, which is caused by the contribution of acoustic modes. It should be noted that (97) is appropriate for the calculation of energy RTs, in the case of mobility a weighted sum including phonon energies and phonon occupation numbers would be more suitable. However, it turns out that there are many combina-

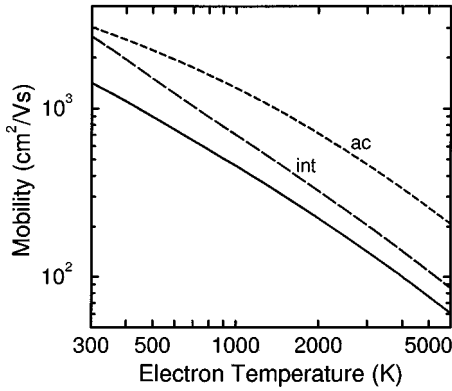


FIG. 13. Electron mobility as a function of carrier temperature at $T_L=300$ K (solid line), and individual contributions of acoustic phonon intravalley (ac) and intervalley scattering (int), respectively.

tions of the couple of parameters $\{D_{int,n}, \hbar\omega_{int,n}\}$ all giving a good fit of $\mu_n(T_L, T_n)$ over a broad range of temperatures. With the choice of $\hbar\omega_{int,n}$, the lattice-mobility curve is “pinned” to the correct room-temperature value with only little influence on the shape of $\mu_n(T_L, T_n)$.

Figure 12 shows $\mu_n(T_L)$ in the range 20 K–500 K (solid line) compared with data points given in Refs. 28, 38–40 and the power law $\mu_n(T_L) = 1417 (T_L/300)^{-2.42}$.⁴¹ Experimental results in the low-temperature range were obtained making corrections for impurity scattering, which partially accounts for the considerable dispersion in the measurements. Our model fits well the results of Ref. 28 over the entire temperature range.

Also shown are the individual contributions of intra- and intervalley scattering (dashed lines), respectively. Intravalley acoustic phonon scattering dominates up to 150 K, whereas comparable contributions are found in the range 200 K–500 K.

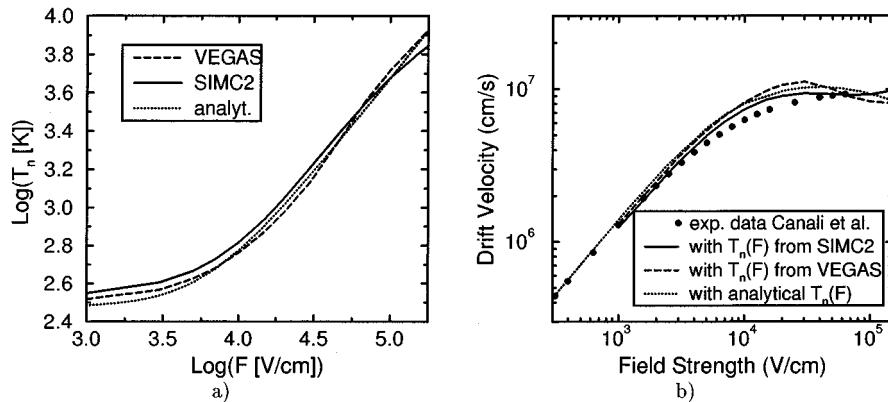


FIG. 14. (a) Average carrier temperature vs electric field from simulations with the MC programs (see Ref. 9) (dashed curve) and (see Ref. 37) (solid curve), and from the analytical relation (98) (dotted curve) with $\tau_{E,n}=0.6$ ps. (b) Electron drift velocity vs electric field with the $T_n(F)$ -relations calculated from (see Ref. 9) (dashed curve) and (see Ref. 37) (solid curve), and from the analytical relation (98) (dotted curve) with $\tau_{E,n}=0.6$ ps. Filled circles: experimental data by Canali *et al.* (see Ref. 42).

C. Dependence on carrier temperature, velocity saturation

Fig. 13 illustrates the dependence of the mobility on carrier temperature at $T_L=300$ K and the individual contributions of acoustic phonon intravalley (ac) and intervalley scattering (int), respectively.

Since hot-carrier mobility data only exist as function of the applied electric field, we need the dependence of carrier temperature on field strength $T_n(F)$. In order to obtain this relation we ran bulk MC simulations with SIMC2⁹ and VEGAS.³⁷ Furthermore, we applied the analytical formula

$$T_n(F) = T_L + \frac{2e}{3k_B} \tau_{E,n} \mu_n(F) F^2, \quad (98)$$

where $\tau_{E,n}$ denotes the energy RT of electrons and $\mu_n(F)$ the heuristic high-field mobility model given by Canali *et al.*⁴² Eq. (98) is the solution of the homogeneous Boltzmann equation in the RTA. The simulated average electron temperatures were then used in the mobility model to compare drift velocity saturation with data from Canali *et al.*⁴² The intervalley scattering parameters $D_{int,n} = 6.68 \times 10^8$ eV/cm and $\hbar\omega_{int,n} = 0.0454$ eV were kept unchanged. Fig. 14 shows the calculated drift velocities. The model reproduces the saturation effect within the uncertainty caused by the $T_n(F)$ -relation. The latter differs between the two MC codes owing to the different band structure models, deformation potential constants, and impact ionization rates. We note that a “perfect fit” could be obtained using Eq. (98) with an adjusted $\tau_{E,n}$ and slightly decreasing the nonparabolicity parameter α .

D. Doping dependence

To improve the fit in the low and intermediate doping range a scaling factor in front of the scattering integral I_{imp} is sufficient. The reason for the calculated electron mobility being systematically larger compared to the experimental data in that range is not clear. This discrepancy was also

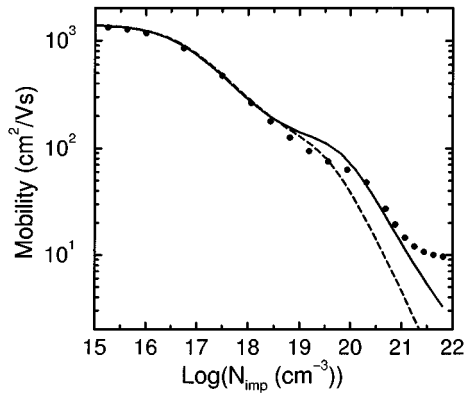


FIG. 15. Electron mobility vs doping calculated with the ideal DOS. Solid curve: without dispersive screening and with I_{imp}^{ndg} [Eq. (62)] scaled by 2.3; dashed curve: with dispersive screening and I_{imp}^{ndg} [Eq. (62)] scaled by 2.2; filled circles: experimental data (see Ref. 26). Parameters: $T_n = T_L = 300$ K, $\alpha = 0.5/eV$.

observed in MC simulations including impurity scattering.^{43,44} Partial wave phase-shift analysis by several authors^{43,45,46} indicated that the drop of the majority carrier mobility is only minor up to $N_{imp} = 10^{18} \text{ cm}^{-3}$. Bennett and Lowney⁴⁷ even found that the Born scattering rate is greater than the phase-shift scattering rate for donor densities less than $2 \times 10^{18} \text{ cm}^{-3}$. On the other hand, it was shown that including the second order perturbation term yields a remarkable drop of the mobility even for the lowest doping concentrations.⁴⁴ Bennett and Lowney⁴⁷ also introduced a scaling factor for the screened Coulomb potential to account for the non-point-ion nature of the electron-donor interaction. They adjusted this factor to yield the measured ground-state binding energy which differs from the result of the hydrogen model when central-cell corrections and valley coupling are neglected. However, it remains open to which extent such a factor can be applied to the continuum states.

In the present model based on the Brooks-Herring theory a constant scaling factor of about 2.2 yields a good agreement with the experimental findings of Masetti *et al.*²⁶ up to 10^{18} cm^{-3} , as shown in Fig. 15. Most likely, a major contribution to this factor originates from short-range electron-electron (e-e) scattering. High-energy carriers which are not much scattered by ionized impurities, lose energy to low-energy carriers that have been scattered by these impurities, resulting in an overall decrease of the mobility. Appel⁴⁸ applied the variational method to an isotropic multi-band model for nondegenerate statistics and derived a numerical curve for the mobility reduction due to e-e scattering in terms of the ratio between electron wavelength and screening length. The reduction factor approaches 0.573 in the high-energy/low-density limit and 1 in the low-energy/high-density limit, respectively. Keyes⁴⁹ and Bate *et al.*⁵⁰ obtained similar factors using the RTA. Keyes⁴⁹ found a strong enhancement of the effect of e-e scattering after addition of anisotropy. According to these results, the use of a constant scaling factor appears as a rather crude approximation and an attempt should be undertaken to incorporate a corrected distribution function into the Brooks-Herring formula that re-

flects the effect of short-range e-e interaction in terms of carrier temperature, density, Fermi statistics and anisotropy.

A further contribution to the required scaling factor 2.2 could be due to electron-plasmon interaction.^{47,51} Fischetti⁵¹ showed the importance of this effect at doping densities above 10^{18} cm^{-3} . For majority electrons its size strongly depends on the assumptions about the dominant decay mechanism. Fischetti considered only plasmons that survive Landau damping long enough to decay mainly by momentum dissipation and randomization, which affects the majority carrier mobility directly. The half-width of the plasmon line was approximated by $\Gamma = \hbar / \langle \tau \rangle$ with $\langle \tau \rangle$ given by the single-particle RT due to phonon and impurity scattering. Using $\langle \tau \rangle = 5 \times 10^{-14} \text{ s}$ a 20% reduction of the electron mobility at $N_D = 10^{19} \text{ cm}^{-3}$ was obtained.

The overestimation of the theoretical mobility around 10^{19} cm^{-3} could be furthermore attributed to multiple-potential scattering.⁴³ At higher densities the mobility is influenced by a variety of additional effects reviewed in Ref. 52, in the first place by dispersive screening, but also by the real DOS as discussed in Section II C 3. For device simulation purposes a practical solution has to be found, because inclusion of additional effects leads to an increase in computation time, which would become unacceptable if, e.g., the real-DOS model (81)–(86) was used. The solid line in Fig. 15 was calculated with the ideal DOS, with I_{imp}^{ndg} given by Eq. (62) and neglecting dispersive screening. However, the good fit in the range $10^{19} \text{ cm}^{-3} - 10^{20} \text{ cm}^{-3}$ is merely a coincidence.

IV. HOLE MOBILITY

A. Band model

The hole spectrum in Si consists of three bands, the heavy and light hole bands which are degenerate at $k=0$, and the split-off band, separated by the spin-orbit energy $\Delta = 0.0443 \text{ eV}$ at $k=0$. All three bands are warped because of the p-like symmetry of the hole Bloch states. Furthermore, they are nonparabolic due to the spin-orbit interaction. The effect of nonparabolicity is largest in the $\langle 110 \rangle$ -direction and at energies near $\Delta/3$.⁵³ Two approximate models are common to calculate macroscopic quantities like DOS, hole concentration, mobility etc.: a two-band model consisting of a spherical nonparabolic heavy band and a spherical parabolic light band, and a one-band model assuming a warped and parabolic heavy band.⁵³

For the purpose of fitting transport data for *p*-type silicon, a temperature dependent isotropic DOS effective mass was calculated for each band in Refs. 54, 55. This was done by equating the hole concentrations obtained with warped, nonparabolic bands to those obtained with a free-electron band model. A polynomial fit for the temperature dependence of the total hole DOS effective mass, based on these calculations, was given in Ref. 56. This temperature dependence originates from an occupation effect and hence, must not be confused with the lattice temperature dependence due to a change in the electron-phonon interaction. The latter is the cause for the temperature dependence of the transverse electron effective mass which was related to the experimentally

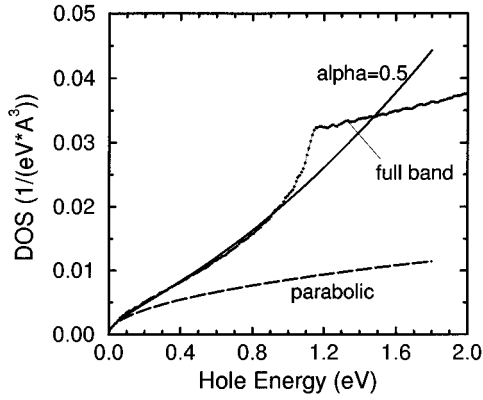


FIG. 16. Hole density of states $D_p(E)$ in silicon. The solid line represents the isotropic, nonparabolic fit model with the DOS effective mass taken for $T_p = T_L = 300$ K and $\alpha = 0.5$ eV. The dotted line is a first-principle full-band result used in the MC program (see Ref. 37). The dashed curve is obtained from the solid line setting $\alpha = 0$.

observed temperature dependence of the gap in Eq. (96). However, in the above mentioned calculations thermodynamic equilibrium ($T_p = T_L$) was assumed. Fig. 16 clearly shows that the isotropic, parabolic model (dashed curves) does not fit to the DOS in the range $k_B T_p$ as the hole temperature increases. Therefore, we will use an isotropic, nonparabolic model with $m_{dp}(T_L)$ in the following and treat the nonparabolicity α as a fit parameter.

A further complication in the calculation of the hole mobility arises from the fact that the p -like symmetry of the hole wave functions results in an angular dependence of the matrix elements. Simplified expressions for the transition probability within the deformation-potential approach include a factor

$$G(\vartheta) = \begin{cases} \frac{1}{4}(1 + 3 \cos^2 \vartheta), & \text{intraband transitions} \\ \frac{3}{4} \sin^2 \vartheta, & \text{interband transitions,} \end{cases} \quad (99)$$

where ϑ denotes the scattering angle.⁵³ For the sake of simplicity, and in accordance with the isotropic band model, we will use the approximation $G(\vartheta) \approx G(0)$ throughout, i.e., also for large-angle scattering. The error will be partly recovered by adjusting the deformation potential constants.

B. Analytical model for the hole mobility

With the above simplifications we may adopt the formulas derived for electrons, replacing electron quantities by the corresponding hole quantities. TA-phonon scattering is negligible due to the symmetry of the hole wave functions. The final form of the hole mobility model reads:

$$\begin{aligned} \mu_p(T_L, T_p, N_{imp}) \\ = \frac{\mu_p^{(0)}(T_L)}{f_{ac}(T_L, T_p) + f_{opt}(T_L, T_p) + f_{imp}(T_L, T_p, N_{imp})}, \end{aligned} \quad (100)$$

with a “scaling” mobility

$$\begin{aligned} \mu_p^{(0)}(T_L) &= \frac{9 e \hbar}{m_{dp}(T_L) k_B T_L} \\ &= 457.2 \left(\frac{300}{T_L} \right) \left(\frac{m_0}{m_{dp}(T_L)} \right) \frac{\text{cm}^2}{\text{Vs}}, \end{aligned} \quad (101)$$

which happens to yield the right order of magnitude (397 cm^2/Vs at room temperature). The terms in the denominator are given by :

$$\begin{aligned} f_{ac} &= 3.53 \times 10^{-4} \left(\frac{m_{dp}(T_L)}{m_0} \right)^{5/2} \sqrt{\frac{300}{T_p}} \\ &\times (1 + 12\tilde{\alpha}) \frac{D_{ac,p}^2}{x_{LA}} e^{-x_{LA}} (1 + \sqrt{8x_{LA}} \sqrt{1 + 8\tilde{\alpha}}), \end{aligned} \quad (102)$$

$$\begin{aligned} f_{opt} &= 1.34 \times 10^{-19} \frac{D_{opt,p}^2}{\hbar \omega_{opt,p}} \sqrt{\frac{T_p}{300}} \left(\frac{m_{dp}(T_L)}{m_0} \right)^{3/2} \left(\frac{300}{T_L} \right) \\ &\times (1 + 12\tilde{\alpha}) \sinh^{-1}(\xi) \xi^2 K_2(\xi), \end{aligned} \quad (103)$$

$$\begin{aligned} f_{imp} &= 5.88 \times 10^{-19} N_{imp} \sqrt{\frac{m_0}{m_{dp}(T_L)}} \left(\frac{300}{T_p} \right)^{3/2} \left(\frac{300}{T_L} \right) \\ &\times \{ [(a_p + 1) E_1(a_p) e^{a_p} - 1] (1 - 4\tilde{\alpha} a_p) \\ &+ 4\tilde{\alpha} E_1(a_p) e^{a_p} \}, \end{aligned} \quad (104)$$

with

$$x_{LA} = \frac{m_{dp}(T_L) c_{LA}^2}{2k_B T_p}, \quad \xi = \frac{\hbar \omega_{opt,p}}{2k_B T_p}, \quad \tilde{\alpha} = \alpha k_B T_p \quad (105)$$

and the screening parameter

$$a_p = \frac{\pi \hbar^2 e^2 Z}{2m_{dp}(T_L) \epsilon_s} \frac{J(\hat{q}, \alpha)}{(k_B T_p)^2} \frac{\partial p}{\partial \eta_p}. \quad (106)$$

C. Dependence on ambient temperature, carrier temperature, and doping

The acoustic deformation potential for holes $D_{ac,p}$ and the effective phonon energy for optical deformation potential scattering $\hbar \omega_{opt,p}$ are adopted from Ref. 53: $D_{ac,p} = 2.2$ eV, $\hbar \omega_{opt,p} = 0.061$ eV. Drift-velocity saturation is best reproduced with a nonparabolicity parameter $\alpha = 0.15$ eV. The only free parameter left, the optical deformation potential $D_{opt,p}$, is fixed by fitting the hole mobility to the measured low-field room-temperature value. This gives $D_{opt,p} = 4.26 \times 10^8$ eV/cm, in good agreement with the parameters of the full-band MC program.³⁷

The resulting dependence on ambient temperature in the range 10 K–500 K is shown in Fig. 17, together with the individual contributions of acoustic and optical phonon scattering, and with experimental data from Refs. 53, 57, 58. The dotted line represents the power law $\mu_p(T_L) = 470.5 (T_L/300)^{-2.2}$ suggested in Ref. 41.

Fig. 18 illustrates the saturation of the hole drift velocity against the experimental data of Canali *et al.*⁴² The hole temperature versus electric field relation was obtained from a bulk MC simulation with VEGAS³⁷ (dots in the left part of

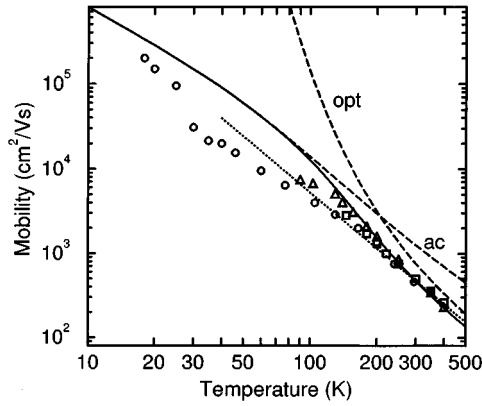


FIG. 17. Hole mobility as a function of lattice temperature (thermalized carriers assumed). Solid line: model of the present paper; dotted line: the power law of Ref. 41; dashed lines: contributions of acoustic phonon (ac) and optical phonon scattering (opt), resp.; triangles: exp. data of Ref. 57; squares: exp. data of Ref. 58; circles: exp. data of Ref. 53.

Fig. 18) and by applying the analytical formula (98) to the case of holes with an energy RT $\tau_{E,p} = 0.25ps$ (solid line in the left part of Fig. 18).

The dependence on doping is shown in Fig. 19 and compared with measurements by Masetti *et al.*²⁶ In the case of holes no scaling factor is necessary to obtain a good fit in the low and intermediate doping range. As in the case of electrons, for concentrations larger than 10^{19} cm^{-3} the calculated mobility strongly depends on the degree of approximation necessary to account for Fermi statistics in the scattering integral. In Fig. 19 the results from Eq. (104) and all effects connected with heavy doping are shown.

V. SIMULATION RESULTS

The model was implemented into the device simulator DESSIS-ISE (Ref. 59) which solves two current-transport equations, two energy-balance equations, Poisson equation and lattice-heat equation. The hard-coded version is given by

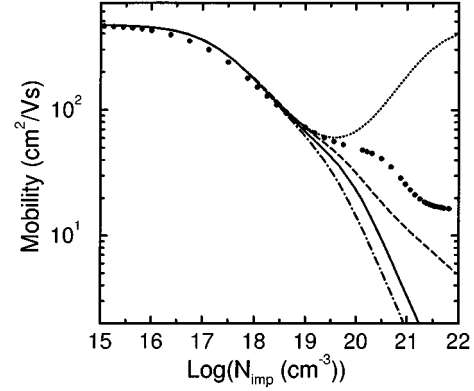
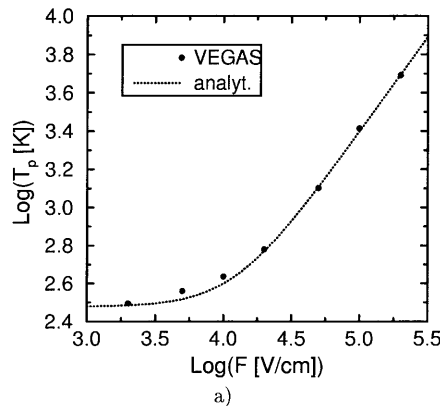


FIG. 19. Hole mobility vs doping calculated with the ideal DOS. Solid curve: without dispersive screening and with I_{imp}^{ndg} corresponding to Eq. (62); dashed curve: without dispersive screening and with numerical I_{imp} corresponding to Eq. (60); dot-dashed curve: with dispersive screening and I_{imp}^{ndg} corresponding to Eq. (62); dotted curve: with nondegenerate statistics in the screening term; filled circles: experimental data (see Ref. 26). No scaling factor in front of the scattering integral has been used. Parameters: $T_p = T_L = 300 \text{ K}$, $\alpha = 0.15/\text{eV}$.

the solid line of Fig. 15 (no dispersive screening, with Fermi statistics in the screening length, ideal DOS). We compare results against those obtained with two other carrier-temperature dependent models. The first has been derived from the Canali model⁴² under homogeneous time-independent conditions:

$$\mu = \frac{\mu_{low}}{[\sqrt{1 + \alpha^2(w_c - w_0)^\beta + \alpha(w_c - w_0)^{\beta/2}}]^{2/\beta}} \quad (107)$$

with $\alpha = [\mu_{low}/(\tau_e v_{sat}^2)]^{\beta/2}$. Here μ_{low} is the default low-field mobility model,²⁶ τ_e is the energy relaxation time, v_{sat} the saturation velocity, w_c the average carrier kinetic energy, and β is the same as for the Canali model. Default parameters have been used for the simulations that can be found in Ref. 59. The second model is similar to the Meinerzhagen-Engl model:⁶⁰

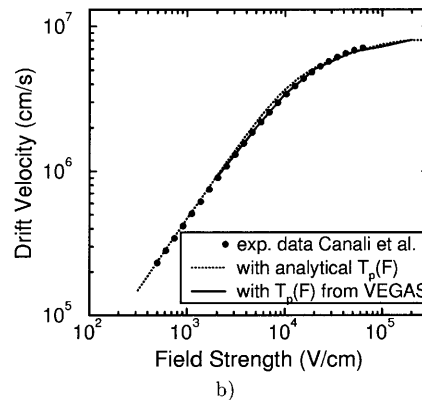


FIG. 18. (a) Average hole temperature vs electric field from simulations with the MC program (Ref. 37) (filled circles) and from the analytical relation corresponding to (98) (dotted curve) with $\tau_{E,p} = 0.25 \text{ ps}$. (b): Hole drift velocity vs electric field with the $T_p(F)$ -relations calculated from Ref. 37 (solid curve) and from the analytical relation corresponding to (98) (dotted curve) with $\tau_{E,p} = 0.25 \text{ ps}$. Parameters: $\alpha = 0.15/\text{eV}$, $D_{ac,p} = 2.2 \text{ eV}$, $D_{opt,p} = 4.26 \times 10^8 \text{ eV/cm}$, and $\hbar \omega_{opt,p} = 0.061 \text{ eV}$. Filled circles: experimental data by Canali *et al.* (see Ref. 42).

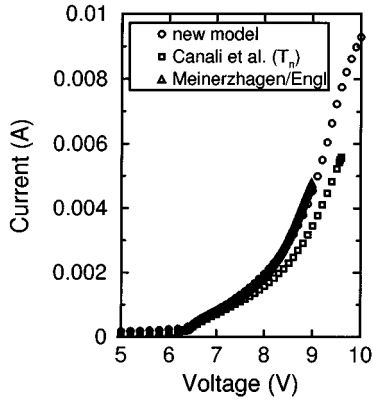


FIG. 20. Simulated IV-characteristics of a *nin*-device with $N_D=2 \times 10^{18} \text{ cm}^{-3}$ in the highly doped *n*-regions and $N_D=2 \times 10^{13} \text{ cm}^{-3}$ in the *i*-region of $1 \mu\text{m}$ width according to different carrier-temperature dependent mobility models.

$$\mu = \frac{\mu_{low}}{\left[1 + \left(\frac{3k_B \mu_{low}}{2e\tau_e v_{sat}} \frac{T_c - T_L}{v_{sat}} \right)^{\beta} \right]^{1/\beta}} \quad (108)$$

Fig. 20 shows IV-characteristics of a *nin*-device with $N_D=2 \times 10^{18} \text{ cm}^{-3}$ in the highly doped *n*-regions and $N_D=2 \times 10^{13} \text{ cm}^{-3}$ in the *i*-region of $1 \mu\text{m}$ width. This figure demonstrates the good convergence behavior of the model in conjunction with the default impact ionization model of Ref. 59. The density of the symbols illustrates the rate of convergence. Fig. 21 shows IV-characteristics of a n^+nn^+ -device with $N_D=2 \times 10^{18} \text{ cm}^{-3}$ in the highly doped n^+ -regions and $N_D=5 \times 10^{16} \text{ cm}^{-3}$ in the lightly doped *n*-region. The treatment of hot-carrier scattering by ionized impurities in the *n*-zone is completely different in the new model, hence one observes a larger variation of the IV-curves for the n^+nn^+ -device, in particular an advanced avalanche breakdown.

Fig. 22 presents source-drain currents as a function of

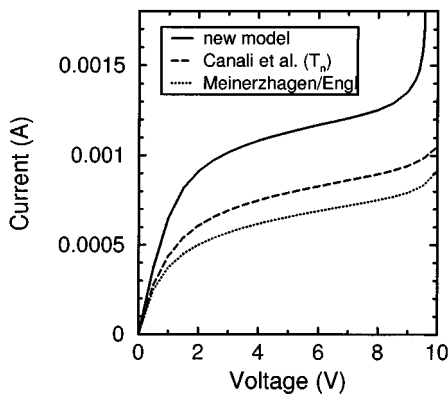


FIG. 21. Simulated IV-characteristics of a n^+nn^+ -device with $N_D=2 \times 10^{18} \text{ cm}^{-3}$ in the highly doped n^+ -regions and $N_D=5 \times 10^{16} \text{ cm}^{-3}$ in the lightly doped *n*-region of $1 \mu\text{m}$ width according to different carrier-temperature dependent mobility models.

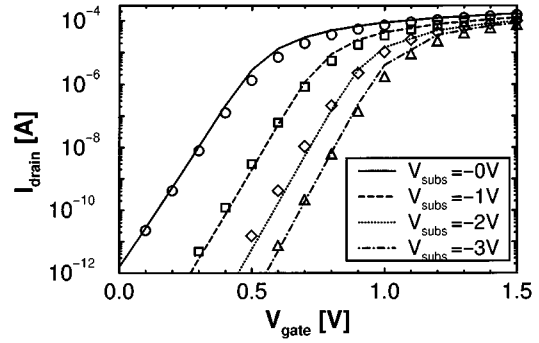


FIG. 22. Drain current versus gate voltage at 0.1 V drain voltage for a $0.5 \mu\text{m}$ -MOSFET produced and measured by Fujitsu. The symbols represent the experimental data, the curves were obtained with the mobility model of this paper.

gate voltage of a $0.5 \mu\text{m}$ -MOSFET at 0.1 V drain voltage for different values of the substrate bias. The MOSFET was fabricated and measured by Fujitsu. The presented mobility model was used in conjunction with the default surface scattering model of Ref. 59. The mesh had 2308 nodes and the increase of total CPU time using the new model was less than 2%.

VI. DISCUSSION

We derived an analytical model for the bulk mobility of electrons and holes in silicon suitable for the implementation in device simulators based on the hydrodynamic transport equations. The mobility is given as a function of carrier temperature, lattice temperature and doping. In the case of degenerate statistics it also depends on the quasi Fermi energies. Analytical integration of the collision terms demanded for a spherical band model, but nonparabolicity was found to be crucial and, therefore, was taken into account throughout the calculation. The adjusted coupling constants—deformation potentials and phonon energies—are in good agreement with effective values obtained from the corresponding sets of deformation potential constants and phonon spectra used in first-principle MC simulations. A good agreement with the measured mobilities in the temperature range 20 K–500 K and for the high-field saturation of the drift velocities was found. The results show that, despite the oversimplified band structure, it is possible to reproduce the nonlinear behavior of the mobility, because the nonparabolicity parameter allows for a sufficient approximation at higher energies.

In the case of scattering from ionized impurities the situation is less satisfactory, particularly in the range of heavy doping. The electron mobility is overestimated by the first-order scattering theory, whereas the hole mobility agrees well with measured data up to the onset of degeneracy. After the discussion of the most important effects related to impurity scattering, it may be argued that the Born approximation fails even for lowly doped *n*-type silicon. This conclusion is supported by the results of MC simulations including first-order scattering with ionized impurities,³⁷ which show the

same overestimation of the mobility in the intermediate doping range, but a sharp drop, when the second order term is taken into account. A constant scaling factor is sufficient to obtain good agreement with experimental data for *n*-type silicon at room temperature up to $N_{imp} = 10^{19} \text{ cm}^{-3}$. However, it remains an open question to which extent the disagreement vanishes as the average carrier energy increases.

Beyond the onset of degeneracy the calculated mobility is rapidly decreasing, if Fermi statistics is applied only to the screening parameter, but using the same analytical form of the scattering integral as in the nondegenerate case. Numerical integration improves the fit, but the modification of the density of states due to heavy doping was found to have an even stronger influence, and is difficult to be accounted for. Both numerical integration and the inclusion of a model for the real DOS lead to an unacceptable increase of the computation time when the model is included in a device simulator. A way out could be to use a fitting function for the screening parameter, which would account for both degeneracy and the real DOS. However, as for the higher perturbation terms, the significance of such a fitting function would become questionable as the average carrier temperature rises under high-field conditions, since the perturbation of the ideal DOS should be most pronounced near the band edges.

ACKNOWLEDGMENTS

The author wishes to thank Dr. A. Benvenuti for implementing the mobility model into the device simulator DESSIS-ISE,⁵⁹ for testing it, and for the critical reading of the manuscript. Thanks also to Dr. P. D. Yoder for providing various MC data, for giving access to his MC programs SIMC2⁹ and VEGAS,³⁷ and for his constructive suggestions and comments. The author is grateful to Dr. N. Sasaki from Fujitsu, Atsugi, Japan for providing experimental data.

¹K. Bløtekjær, IEEE Trans. Electron Devices **ED-17**, 38 (1970).

²R. Stratton, Phys. Rev. **126**, 2002 (1962).

³C. Jacoboni and L. Reggiani, Rev. Mod. Phys. **55**, 645 (1983).

⁴D. Ventura, A. Gnudi, G. Baccarani, and F. Odeh, Appl. Math. Lett. **5**, 85 (1992).

⁵M. Kohler, Z. Physik **124**, 772 (1947).

⁶J. M. Ziman, *Electrons and Phonons* (Oxford University Press, Oxford, 1960).

⁷M. Asche and O. G. Sarbei, Phys. Status Solidi **33**, 9 (1969).

⁸K. Hess, "Phenomenological Physics of Hot Carriers in Semiconductors," in *Physics of Nonlinear Transport in Semiconductors*, edited by D. K. Ferry, J. R. Barker, and C. Jacoboni (Plenum, New York, 1980), Vol. 52, pp. 1–42.

⁹H. Shichijo, J. Y. Tang, J. Bude, and D. Yoder, "Full Band Monte Carlo Program for Electrons in Silicon," in *Monte Carlo Device Simulation: Full Band and Beyond*, edited by Karl Hess (Kluwer Academic, Boston, 1991), Chap. 10, pp. 285–307.

¹⁰R. Thoma, A. Emunds, B. Meinerzhagen, H. J. Peifer, and W. L. Engl, IEEE Trans. Electron Devices **ED-38**, 1343 (1991).

¹¹C. Herring and E. Vogt, Phys. Rev. **101**, 944 (1956).

¹²D. L. Rode, Phys. Status Solidi B **53**, 245 (1972).

¹³R. Kubo, J. Phys. Soc. Jpn. **12**, 570 (1957).

¹⁴D. A. Greenwood, Proc. Phys. Soc. London **71**, 585 (1957).

¹⁵*Basic Properties of Semiconductors*, edited by P. T. Landsberg (North-Holland, Amsterdam, 1992), Vol. 1.

¹⁶A. Schenk, Phys. Status Solidi A **122**, 413, 723 (1990).

¹⁷N. Takimoto, J. Phys. Soc. Jpn. **14**, 1142 (1959).

¹⁸H. Fröhlich and V. Paranjape, Proc. Phys. Soc. London B **69**, 21 (1956).

¹⁹R. Stratton, Proc. Roy. Soc. London A **242**, 355 (1957).

²⁰H. G. Reik and H. Risken, Phys. Rev. **124**, 777 (1961).

²¹B. R. Nag, Solid-State Electron. **10**, 385 (1967).

²²E. M. Conwell, *High Field Transport in Semiconductors*, Volume 9 of *Solid State Physics* (Academic, New York, 1967).

²³K. Blotekjaer and E. B. Lunde, Phys. Status Solidi **85**, 581 (1969).

²⁴M. Abramowitz and I. A. Stegun, *Handbook of Mathematical Functions with Formulas, Graphs, and Mathematical Tables* (Dover, New York, 1972).

²⁵R. Zimmermann, *Many Particle Theory of Highly Excited Semiconductors*, Texte zur Physik, Band 18 (BSB Teubner Verlagsgesellschaft, Leipzig, 1988).

²⁶G. Masetti, M. Severi, and S. Solmi, IEEE Trans. Electron Devices **ED-30**, 764 (1983).

²⁷A. G. Samoilovich, I. Y. Korenblit, and I. V. Dakhovskii, Sov. Phys. Dokl. **6**, 606 (1962).

²⁸P. Norton, T. Braggins, and H. Levinstein, Phys. Rev. B **8**, 5632 (1973).

²⁹J. M. Ziman, *Elements of Advanced Quantum Theory* (Cambridge University Press, New York, 1969).

³⁰E. O. Kane, Phys. Rev. **131**, 79 (1963).

³¹T. N. Morgan, Phys. Rev. A **139**, 343 (1965).

³²S. Selberherr, *Analysis and Simulation of Semiconductor Devices* (Springer, Wien, 1984).

³³G. L. Pearson and J. Bardeen, Phys. Rev. **75**, 865 (1949).

³⁴P. P. Debye and E. M. Conwell, Phys. Rev. **93**, 693 (1954).

³⁵D. B. M. Klaassen, Solid-State Electron. **35**, 953 (1992).

³⁶M. A. Green, J. Appl. Phys. **67**, 2944 (1990).

³⁷P. D. Yoder, Ph.D. thesis, University of Illinois, Urbana, Illinois, 1994.

³⁸D. Long, Phys. Rev. **120**, 2024 (1960).

³⁹C. J. Rauch, J. J. Stickler, H. J. Zeiger, and G. S. Heller, Phys. Rev. Lett. **4**, 64 (1960).

⁴⁰R. A. Logan and A. J. Peters, J. Appl. Phys. **31**, 122 (1960).

⁴¹C. Lombardi, S. Manzini, A. Saporito, and M. Vanzi, IEEE Trans. CAD **7**, 1164 (1988).

⁴²C. Canali, G. Majni, R. Minder, and G. Ottaviani, IEEE Trans. Electron Devices **ED-22**, 1045 (1975).

⁴³L. E. Kay and T. W. Tang, J. Appl. Phys. **70**, 1475 (1991).

⁴⁴P. D. Yoder, Integrated Systems Laboratory, ETH Zurich (private communication).

⁴⁵F. J. Blatt, J. Phys. Chem. Solids **1**, 262 (1957).

⁴⁶J. R. Meyer and F. J. Bartoli, Phys. Rev. B **23**, 5413 (1981).

⁴⁷H. S. Bennett and J. R. Lowney, J. Appl. Phys. **71**, 2285 (1992).

⁴⁸J. Appel, Phys. Rev. **125**, 1815 (1961).

⁴⁹R. W. Keyes, J. Phys. Chem. Solids **6**, 1 (1958).

⁵⁰R. T. Bate, R. D. Baxter, F. J. Reid, and A. C. Beer, J. Phys. Chem. Solids **26**, 1205 (1965).

⁵¹M. V. Fischetti, Phys. Rev. B **44**, 5527 (1991).

⁵²D. Chattopadhyay and H. J. Queisser, Rev. Mod. Phys. **53**, 745 (1981).

⁵³G. Ottaviani, L. Reggiani, C. Canali, F. Nava, and A. Alberigi-Quaranta, Phys. Rev. B **12**, 3318 (1975).

⁵⁴H. D. Barber, Solid-State Electron. **10**, 1039 (1967).

⁵⁵F. L. Madarasz, J. E. Lang, and P. M. Hemeger, J. Appl. Phys. **52**, 4646 (1981).

⁵⁶J. E. Lang, F. L. Madarasz, and P. M. Hemeger, J. Appl. Phys. **54**, 3612 (1983).

⁵⁷G. W. Ludwig and R. L. Watters, Phys. Rev. **101**, 1699 (1956).

⁵⁸F. J. Morin and J. P. Maita, Phys. Rev. **96**, 28 (1954).

⁵⁹S. Müller, K. Kells, A. Benvenuti, J. Litsios, U. Krumbein, A. Schenk, and W. Fichtner, DESSIS 1.3.6: Manual, ISE Integrated Systems Engineering AG, Zürich (1994).

⁶⁰B. Meinerzhagen and W. L. Engl, IEEE Trans. Electron Devices **35**, 689 (1988).